Review
doi.org/10.1002/batt.202200486
Chemistry Europe
European Chemical Societies Publishing

www.batteries-supercaps.org

Review on Cathode Materials for Sodium- and Potassium-Ion Batteries: Structural Design with Electrochemical Properties

Hyunyoung Park,[a, b] Yongseok Lee,[a, b] Wonseok Ko,[a, b] Myungeun Choi,[a, b] Bonyoung Ku,[a, b] Hobin Ahn,[a, b] Junseong Kim,[a, b] Jungmin Kang,[a, b] Jung-Keun Yoo,[c] and Jongsoon Kim*[a, b]

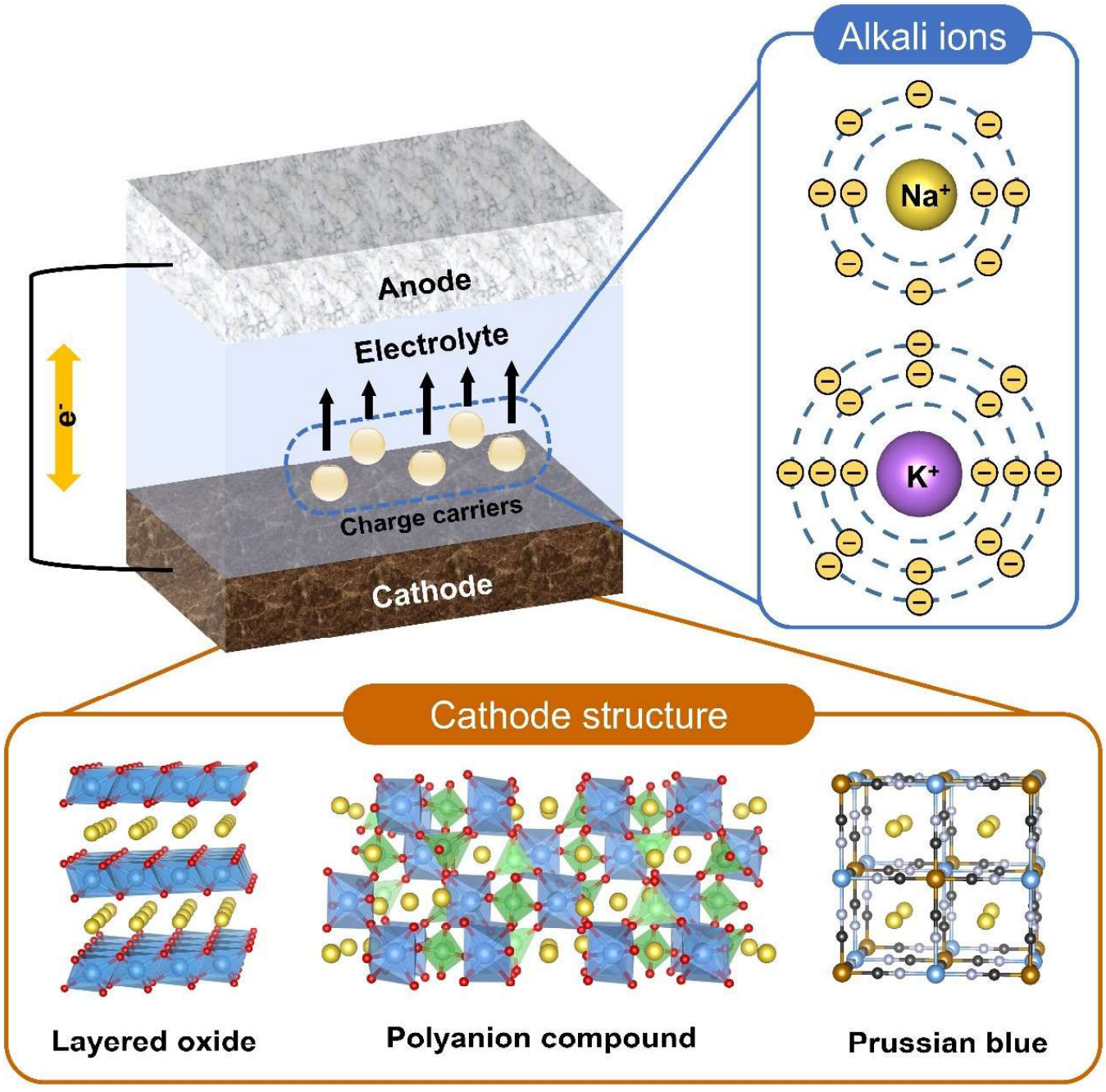

As a promising candidates for next-generation secondary battery system, sodium-ion (Na-ion) batteries and potassium-ion (K-ion) batteries are recently attracting considerable attention because of their cost-effectiveness and similar reaction mechanism to that of lithium-ion batteries. However, the major challenges for their practical application are sluggish ionic kinetic with excessive volume change of the cathode material, caused by larger ionic radius than Li^+ ion. The current demand for high energy density is not satisfactory with the electrochemical properties of the cathode materials for Na-ion and K-ion batteries studied so far, but extensive studies have been conducted to achieve large reversible capacity, high power capacity, and long life in recent years. This review provides comprehensive information on the cathode material studies reported to date for Na-ion and K-ion batteries, with a particular focus on the various strategies of each cathode material to achieve high electrochemical properties. In this regard, diverse electrochemical properties of cathode materials for Na-ion and K-ion batteries are compared with current Li-ion battery systems, and future research directions are discussed along with related challenges and prospects.

1. Introduction

Environmental issues are currently of great concern, and the use of eco-friendly and sustainable energy sources is encouraged to address issues such as global warming and abrupt climate change.[1,2] Such energy sources, including solar energy, wind energy, and hydroelectric energy, are attractive for natural power generation, which is more environmental friendly than the use of fossil fuels; nevertheless, they are not yet widely used due to the limitation of intermittent production.[3] To overcome this problem, energy storage systems (ESSs) are introduced, which resolves the imbalance in power generation for green energy and enables a stable power supply. The secondary battery applied to ESSs requires high energy density with high power capability. Among various candidates, lithium-ion batteries (LIBs) are considered suitable for this purpose, as they are capable of supplying large amounts of energy in a short time. LIBs were first commercialized in 1991, with further development over the last three decades resulting in higher energy density along with improvements in cathode materials such as $LiCoO_2$ and $LiNi_xCo_yMn_zO_2$ (NCM).[4–6] However, the COVID-19 pandemic has resulted in soaring of the price of lithium raw materials due to the absence of supply-chain expansion, with the rapid growth of industries accelerating this trend, resulting in the need for large-capacity secondary batteries such as ESSs and electric vehicles.[7,8]

Among the numerous candidates to replace LIBs, sodium-ion batteries (NIBs) have regarded as one of the most promising batteries due to the following potential advantages. First, as one of the most attractive advantages, the cost of sodium resources is very low compared to lithium resources. Unlimited and abundance reserves without any geographical restriction allows the Na resources to possess competitive cost than other minerals. In the earth's crust, the relative abundance of lithium element only occupied as 20 ppm (even the reserves are concentrated in Latin America), whereas Na element occupied as 23,600 ppm, indicating that sodium is the sixth most common element in the earth.[9–12] Based on abundant reserves, the cost of Na_2CO_3 is nearly 300 times lower compared to Li_2CO_3 (Na_2CO_3: 250 USD/ton, Li_2CO_3: 74,310 USD/ton in October 2022), representing the superior cost competitiveness of NIBs.[13] Second, NIBs have suitable energy density competitive to LIBs. Although the redox potentials of sodium ion (Na^+/Na: −2.71 V vs. the standard hydrogen electrode or SHE) is higher than that of lithium ion (Li^+/Li: −3.04 V vs. SHE), NIBs still can be considerable promising batteries with remarkable redox potential when compared to other candidates such as magnesium-ion batteries (Mg^{2+}/Mg: −2.27 V *vs.* SHE).[14–16] Considering that the energy density is calculated as average operation voltage with specific capacity, NIBs belong to high energy density group among various types of batteries, and the energy density of NIBs is gradually increasing through numerous researches.[17,18] Third, reaction mechanism of NIBs is similar with LIBs; Both LIBs and NIBs consist of cathode/anode electrodes, electrolyte and separator. During charge and discharge process, the alkali ions (Li^+ or Na^+) reversibly migrate between cathode and anode electrode. This similar reaction mechanism between LIBs and NIBs enables facilitated replacement or application from conventional LIB industries to NIB system.[19,20]

Unlike NIBs drew highlighted academic and commercial attention through numerous studies since early 2010s, potassium-ion batteries (KIBs) have received less attention to these days. Despite of neglect for a long time, KIBs have a potential with a several inherent merits to be promising cathode. Although not as low as cost of sodium, the cost of potassium is also fairly low (K_2CO_3: 1000 USD/ton at Oct. 2022) based on abundant reserves as 20,900 ppm which is the seventh most common element in the earth.[9–13] In addition, potassium ion have the lower redox potentials (K^+/K: −2.93 V vs. SHE), which is the only ~0.1 V above that of lithium ion.[14–16] Furthermore, not only reaction mechanism is similar between KIBs and LIBs as the alkali-ion batteries, but also conventional graphite can be used as anode of both batteries. Graphite is the most widespread anode material in LIBs system, and potassium ions can intercalate into the graphite structure forming a one-stage KC_8 at a low potential, which delivers a satisfactory theoretical

[a] H. Park, Y. Lee, W. Ko, M. Choi, B. Ku, H. Ahn, J. Kim, J. Kang, Prof. J. Kim
Department of Energy Science, Sungkyunkwan University, Suwon, 16419, Republic of Korea
E-mail: jongsoonkim@skku.edu
[b] H. Park, Y. Lee, W. Ko, M. Choi, B. Ku, H. Ahn, J. Kim, J. Kang, Prof. J. Kim
SKKU Institute of Energy Science and Technology (SIEST), Sungkyunkwan University, Suwon, 16419, Republic of Korea
[c] Dr. J.-K. Yoo
Carbon Composites Department, Composites Research Division, Korea Institute of Materials Science (KIMS), 797 Changwondaero, Changwon, 51508, Republic of Korea

capacity of ~279 mAh g^{-1}.[21,22] This is the unique feature of the KIBs over the NIBs, because there are no previous reports that Na^+ ions could intercalated into graphite with carbonate-based electrolyte. Therefore, in terms of application based on conventional LIB industry, it was considered that KIBs are more suitable than NIBs.

Although NIBs and KIBs exhibit promising potentials to adopted on large-scale energy storage devices, there is inherent obstacles that need to overcome for application in practical battery industries. The one of the most crucial issues is the large ion radius of Na and K ion compared to that of Li ion (Li^+: 0.76 Å, Na^+: 1.02 Å and K^+: 1.38 Å), which results in severe structural degradation and irreversible phase transition.[23,24] Thus, sluggish kinetics, excessive volume changes and drastic capacity fading occur during the repeated charge/discharge process.[25,26] Moreover, as mentioned above, the higher redox potentials of NIBs and KIBs are also inevitable problems to following the excellent energy density of LIBs. Therefore, it is necessary to explore the recent trends of studies for NIBs or KIBs, which are the most potential candidates to satisfy the high demand for the development of next-generation cathode materials.

In this review, we present an overview of recent studies on various cathode materials for NIBs and KIBs. First, we discuss

Hyunyoung Park is currently a Ph.D candidate in the Department of Energy Science at Sungkyunkwan University. He received master's degree in Nano Engineering from Sejong University in 2018. His research focuses on development of cathode materials for high-performance alkali-ion batteries.

Yongseok Lee is currently a Ph.D candidate in the Department of Energy Science at Sungkyunkwan University. He received master's degree in Nanotechnology and Advanced Materials Engineering from Sejong University in 2020. His research focuses on development of cathode materials for high-performance alkali-ion batteries.

Wonseok Ko is currently a Ph.D candidate in the Department of Energy Science at Sungkyunkwan University. He received master's degree in Nanotechnology and Advanced Materials Engineering from Sejong University in 2020. His research focuses on development of cathode materials for high-performance alkali-ion batteries.

Myungeun Choi is currently a integrated M.S./Ph.D candidate in the Department of Energy Science at Sungkyunkwan University. Her research focuses on development of Mn-based cathode materials for high-performance sodium-ion batteries.

Bonyoung Ku is currently a integrated M.S./Ph.D candidate in the Department of Energy Science at Sungkyunkwan University. His research focuses on development of Mn-based cathode materials for high-performance sodium-ion batteries.

Hobin Ahn is currently a integrated M.S./Ph.D candidate in the Department of Energy Science at Sungkyunkwan University. His research focuses on development of Mn-based cathode materials for high-performance sodium-ion batteries.

Junseong Kim is currently a integrated M.S./Ph.D candidate in the Department of Energy Science at Sungkyunkwan University. His research focuses on development of Li-rich layered oxide cathode materials for high-performance lithium-ion batteries.

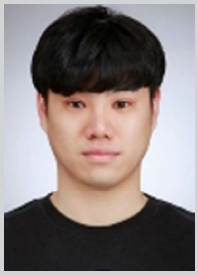

Jungmin Kang is currently a Ph.D candidate in the Department of Energy Science at Sungkyunkwan University. He received master's degree in Nanotechnology and Advanced Materials Engineering from Sejong University in 2021. His research focuses on development of various electrode materials for high-performance alkali-ion batteries.

Jung-Keun Yoo is a senior researcher of Carbon Composites Department in Korea Institute of Materials Science (KIMS). He obtained his MSc and PhD at the Korea Advanced Institute of Science and Technology (KAIST). His research focuses on development of new conductive material and binder for next-generation secondary batteries.

Jongsoon Kim is an assistant professor of the Department of Energy Science in Sungkyunkwan University. He obtained his BSc and MSc at the Korea Advanced Institute of Science and Technology (KAIST). Then, he completed his PhD (2014) at Seoul National University. His research laboratory focuses on development of new materials for Li-ion and Na-ion batteries using ab initio calculations and X-ray/neutron-based analyses.

the fundamental information of cathode materials, which are categorized into layered metal oxides, polyanion-based compounds, and Prussian blue analogues. Next, recent progress and developments in cathode materials will be reviewed, including the synthesis methods, electrochemical properties and various analyses techniques. Finally, the main challenges faced by these cathode materials are summarized, and future research direction and prospects are presented in consideration of their practical application.

2. Classification of the Structures of Cathode Materials

As mentioned, the structure of the cathode material could be broadly classified into three types: layered metal oxides, polyanion-based compounds, and Prussian blue analogues (Figure 1). Each structure has its own unique properties, and numerous investigations have been conducted as promising cathode materials candidates for post-LIBs.

Layered metal oxides consist of alternating layers of edge-sharing transition metal oxide (MO_6) layers and alkali-metal layers along the *c*-axis, and they possess a higher energy density than other cathode materials due to dense packing structure. In addition, widely arranged two-dimensional space for the alkali-ion allows fast ion diffusion, enabling high rate performance in battery systems. The layered metal oxides are further classified by the coordination of the alkali ions into either P-type (prismatic) or O-type (octahedral). Generally, the P-type structure exhibits high ionic conductivity with stable structural change, which is attributed to the thermodynamically stable prismatic ion site.[27,28] However, this structure is difficult to apply in the industrial field because of the deficient alkali-ion concentration. On the other hand, the O-type structure can deliver high specific capacity with sufficient alkali-ion content; however, it provides limited rate-capability because of the complex ionic diffusion between the original octahedral site and intermediate tetrahedral site.[29,30] In addition, compared with the P-type structure, cations in the transition-metal layer more readily migrate to the face-shared tetrahedral site in the alkali-metal layer (i.e. cation migration), leading to severe irreversible structural transformation and poor cyclability. These classifications are further subdivided according to the stacking order, which determines the crystal structure, such as P2 or O3. Given the larger ionic radius of Na^+ and K^+, the coordination positions of alkali ions in layered oxide materials differ significantly from those in the LIB system.

Polyanion-based compounds have XO_4 (X=P, S, etc.) polyanions in the crystal structure, which exhibit strong covalent bonding with the transition metal, leading to high structural stability.[31,32] In addition, the polyanion framework increases the redox potential of the transition metal, which is called the inductive effect. The high-electronegativity X atom weakens the M–O covalent bonds and reduces the energy gap between the anti-bonding and bonding orbitals. In contrast, it forms a larger energy gap with the redox couple of the alkali ion, leading to higher cell voltage.[33,34] Nevertheless, the low electrical conductivity must be addressed; thus, various modification methods have been introduced such as nano-sizing of particles, conductive carbon coating, and morphology optimization.

Prussian blue and its analogues are metal-organic frameworks (MOFs) with the chemical formula $A_xM[Fe(CN)_6]_y \cdot nH_2O$ ($0 \le x \le 2$, $y \le 1$), where A is an alkali metal and M is a transition metal.[35–37] Each transition metal occupying an octahedral site is bonded with a cyanide ligand (–CN–), forming a structure with large interstitial sites capable of accommodating larger

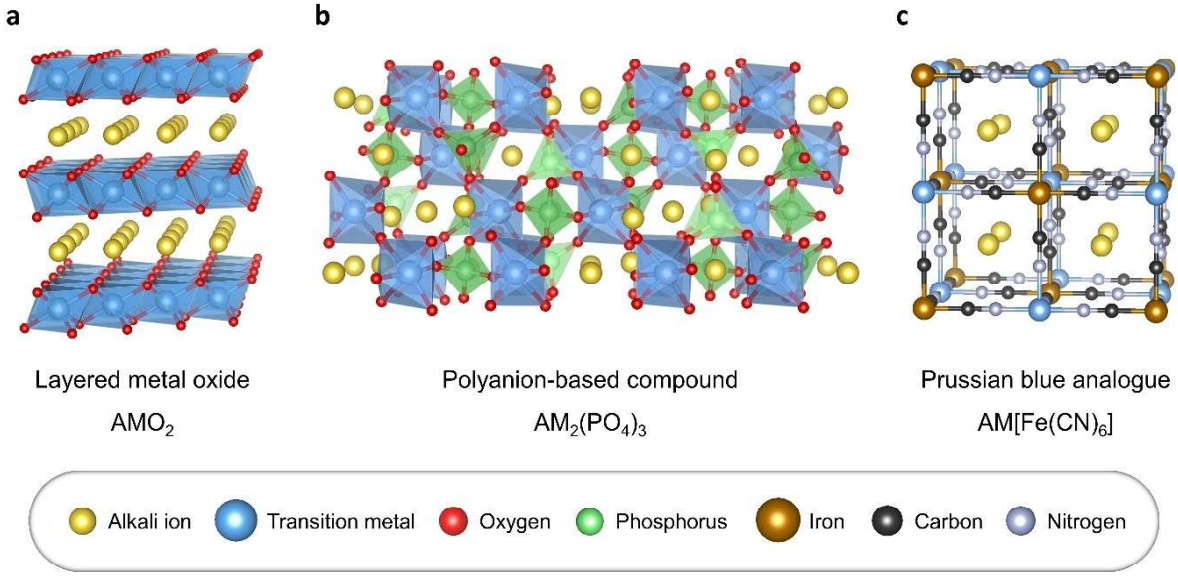

Figure 1. Representative crystal structures of cathode materials. a) layered metal oxide AMO_2, b) polyanion-based compound $AM_2(PO_4)_3$ and c) Prussian blue analogue $AM[Fe(CN)_6]$.

alkali ions. This crystal structure effectively alleviates the volume expansion during cycling, providing a significantly longer lifespan than for other cathode materials.[38,39] Although they can be facilely synthesized at low cost, additional treatments such as particle-size control with lattice-defect control are required to achieve higher electrochemical performance. In particular, the degree of incorporation of crystalline water molecules varies depending on the synthesis conditions, which lowers the operating voltage and inhibits the storage of alkali ions.[40]

Besides the three types of cathode materials described above, organic-base cathode materials are also receiving great attention. Compared with commonly used inorganic-based cathode materials, organic-based materials are mainly composed of low atomic weight elements (C, H, O, etc.), which enables the low-cost synthesis. The molecular structure can be designed flexibly through substitution of various functional groups, and a large number of alkali ions can be stored through widely distributed redox-active sites.[41–43] On the other hand, volumetric energy density is relatively lower than other cathode material, which is unfavorable for practical application.[44,45]

The average voltage, specific capacity, and energy density of recently reported cathode materials are summarized in Figure 2.[46–108] In the NIB system, layered oxide cathode was found to be more advantageous in overall electrochemical properties, including the gravimetric capacity and energy density. In particular, several layered oxide cathodes show high energy densities of over 600 Wh kg^{-1}, showing performance comparable to those of LIBs. Nevertheless, in KIB system, these structure type of cathode exhibited poor electrochemical properties, not only average working voltage but also specific capacity. It is considered that larger K^+ ions increased the distance of K layer, which reduce the screening effect from adjacent oxygen anions.[109,110] In case of polyanion-based cathodes, three-dimensional space for alkali ions separates each ion, and effectively inhibits Na^+–Na^+ and K^+–K^+ interactions. As a result, polyanion-based cathodes provide stable voltage slopes with high voltage during the cycle. However, these materials exhibited low specific capacity because of the large atomic weight of polyanions such as phosphate (PO_4) or sulfate (SO_4). Thus, they delivered lower energy density than other type of cathode materials. Prussian blue analogue cathodes show excellent performance especially in KIB system, which is related to preference for K^+ ions. According to the first-principles calculation, the energetically favorable intercalation site for K^+ ions is the body-centered 8c site, which is the largest interstitial site in Prussian blue analogues. On the other hand, narrower face-centered 24d site was energetically preferred in case of Na^+ ions.[111] It was thought that large interstitial spaces of the Prussian blue analogues are more favorable for storage of K^+ ions, effectively lowering the Gibbs free energy and providing higher operating voltages. However, higher electrochemical properties could only be achieved in Prussian blue analogue structure with low defect or residual moisture.

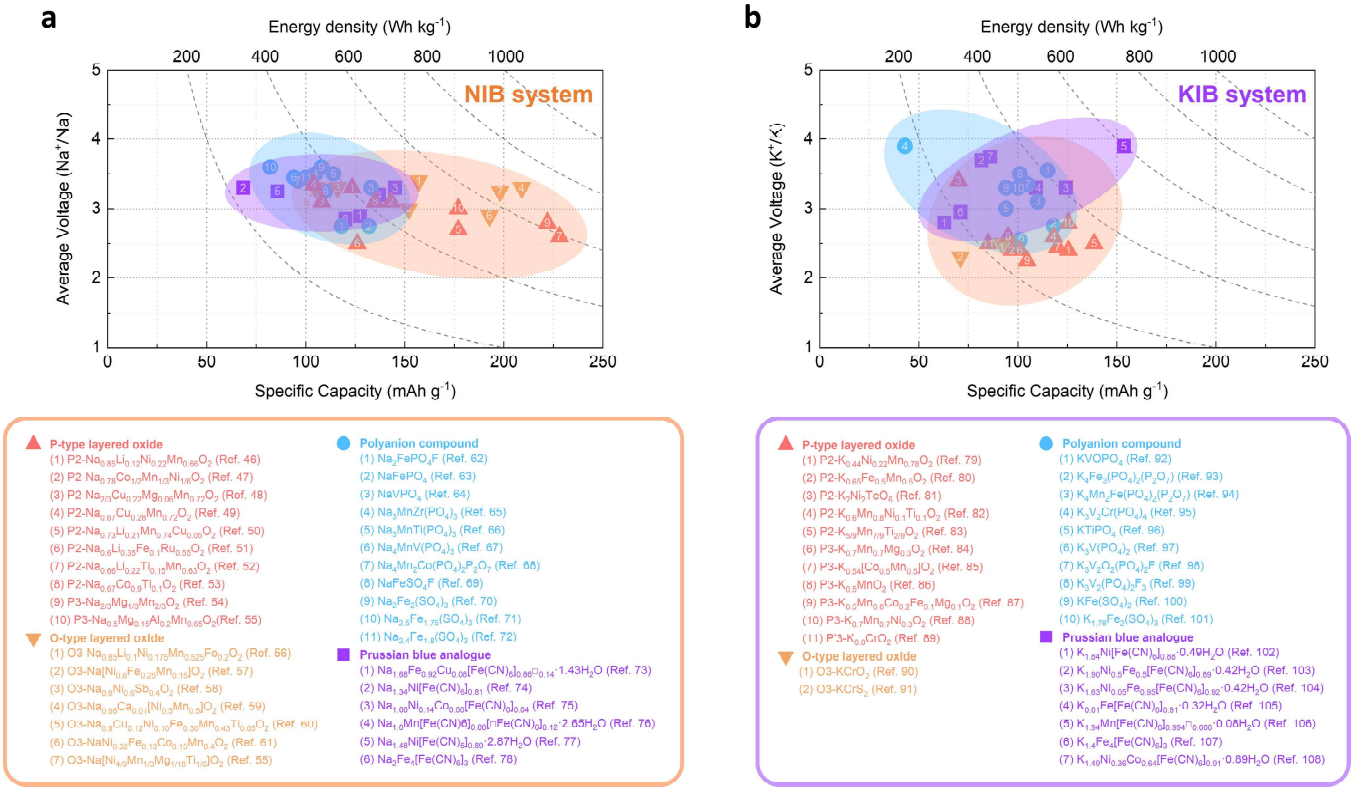

Figure 2. Comparison of electrochemical performances among the cathode materials for a) NIB system and b) KIB system to date.[46–108]

3. Cathode Materials for Na-Ion Batteries

3.1. Layered oxides

In layered oxides in the NIB system, not only the P2 structure but also the O3 structure is preferred, which is determined by the initial number of Na^+ in the synthesis process.[112] Recently, various studies on layered oxide cathode materials have been conducted, with numerous studies on ternary and quaternary metal-based cathode materials to improve the electrochemical performance. Moreover, there are many attempts to apply the reversible anionic redox reactions of O^{2-}/O^{1-} to NIB, proposed in LIB systems to overcome capacity limits in conventional cationic reaction cathode. These approaches are effective in suppressing irreversible structural distortions, increasing the average redox potential, and achieving additional specific capacity.

Hakim et al. reported the energy-storage mechanism of P2–$Na_{0.78}Co_{1/2}Mn_{1/3}Ni_{1/6}O_2$, which exhibited both cationic and anionic redox reaction without the existence of excess Na^+ ion.[47] In this study, the cobalt element was substituted to nickel and manganese for the structural stability for anionic redox voltage region. In the range of 2.0–4.5 V, it delivered a discharge capacity of ~143 mAh g^{-1} while maintaining the P2 structure, providing an additional capacity of ~25 mAh g^{-1} compared to that for the 4.2 V cutoff. To verify the origin of additional capacity with anionic redox reaction, O K-edge X-ray absorption spectroscopy (XAS) analyses were performed. As shown in Figure 3(a), the additional capacity was observed to originate from the redox reaction of oxygen anions. Generally, the pre-edge peak below 534 eV is associated with the transition of O 1s electrons to the hybridized state of M 3d and O 2p orbitals, whereas the broad peak above 535 eV is associated with the transition of O 1s electrons to the hybridized state of M 4 s/4p and O 2p orbitals.[113–115] Thus, it is a strong evidence that this ternary composition induced the anionic redox reaction, accompanying the Co^{4+} and Ni^{4+} oxidation.

Hu et al. introduced Li/Cu co-substitution into the P2-type layered structure to achieve reversible anionic redox reaction in the high-voltage range.[50] The P2–$Na_{0.73}Li_{0.21}Mn_{0.74}Cu_{0.05}O_2$ has Na-O–Li configurations in crystal structure, which activates oxygen redox through O 2p non-bonding orbital.[116] Also, the Cu dopant plays a key role to stabilize this anion redox reaction through the strong covalent bonding with oxygen.[48] In the range of 1.5–4.5 V, it delivered a capacity of ~177 mAh g^{-1} at C/20, with 89.7% of the initial capacity maintained after 90 cycles at 2 C. Besides, the Cu-free P2–$Na_{0.63}Li_{0.21}Mn_{0.79}O_2$ shows capacity retention of 76.3% after 80 cycles under the same current density, implying the poor structural stability. Electron paramagnetic resonance (EPR) spectroscopy was performed to confirm the effect of Cu substitution. During the Na^+ deintercalation, the intensity of the broad peak at $g \approx 1.99$, which related to the $Mn^{(4+)}$–O bond, gradually decreased, indicating the anionic redox reaction with formation of the peroxo-like O–O dimer. In addition, in the magnetic field range of 550–900 mT, a number of signal for the formation of O_2 molecules were observed in the 4.5 V-charged co-free sample, whereas this phenomenon was not observed in 4.5 V-charged P2–$Na_{0.73}Li_{0.21}Mn_{0.74}Cu_{0.05}O_2$. Thus, it was considered that irreversible oxygen release was suppressed through the Cu doping (Figure 3b).

In order to achieve reversible anionic redox reaction, a strategy of doping with two other electrochemically inactive elements was also attempted. Jia et al. developed an Mg and Al co-doped P3-type structure $Na_{0.5}Mg_{0.15}Al_{0.2}Mn_{0.65}O_2$.[117] In the range of 2.0–4.5 V, it delivered 177 mAh g^{-1} of initial discharge capacity at a current rate of 10 mA g^{-1}, corresponding to 0.65 mol Na^+ de/intercalation. In addition, it retained ~82% of initial capacity after the 100 cycles measured at 200 mA g^{-1}, suggesting the improved structural stability through the co-doped effect of electrochemical-inactive elements. *Operando* X-ray diffraction (XRD) analysis was performed to confirm structural changes during cycling (Figure 3c). The peaks corresponding to the (003) and (006) planes shifted to a lower angle during charge, indicating an increase in c parameter due to the repulsive force between oxygen layers with decrease in sodium content in the crystal structure.[118] However, no additional peak shifts or phase transitions were observed in the high voltage region. Concomitant with the total de/intercalation of 0.65 mol Na^+, the crystal structure was maintained with reversible peak shifting during the subsequent charge and discharge. In addition, *ex-situ* differential electrochemical mass spectrometry (DEMS) revealed the structural stability of $Na_{0.5}Mg_{0.15}Al_{0.2}Mn_{0.65}O_2$. CO_2 and O_2 evolution were observed at the first charge, indicating the decomposition of the electrolyte/Na_2CO_3 and the formation of the O–O dimer, respectively. However, little oxygen evolution was detected during the second discharge, whereas CO_2 evolved from Na_2CO_3 decomposition, indicating the stable anionic redox reaction after the second cycle.

As part of suppressing the excessive volume expansion during the structural change of the O3-type structure, structural design with cation disordering in transition metal layer have been reported.[119,120] Yu et al. prepared Ni-based O3-type layered structure with various Sb dopant concentrations to enhance the electrochemical performance.[58] Among the various structures, O3–$Na0.8Ni_{0.6}Sb_{0.4}O_2$ with a cation ratio of 3:2 exhibited complete cation disorder. It delivered a capacity of 116 mAh g^{-1} at 0.1 C (~12 mA g^{-1}), and capacity retention of ~78% was achieved after 100 cycles at 1 C (120 mA g^{-1}). The structural change was measured using *operando* XRD (Figure 3d). During the charge process, (003) and (006) peaks shifted toward the lower angle, whereas (101) and (012) peaks shifted toward high angle. The phase transition from O3 to P3 was clearly observed at ~3.3 V, then a gradual change to P3′ and P3″ phases by additional Na^+ deintercalation and a new hydration peak according to the widened slab space appeared. Interestingly, the change in volume during the reversible O3–P3 phase transition was only ~1%, which was attributed to cation disorder property.

Another co-doping strategy was applied to the Co-free Ni/Mn-based O3 phase structure to suppress excessive structural changes and consequent capacity decay. Kubota et al. reported

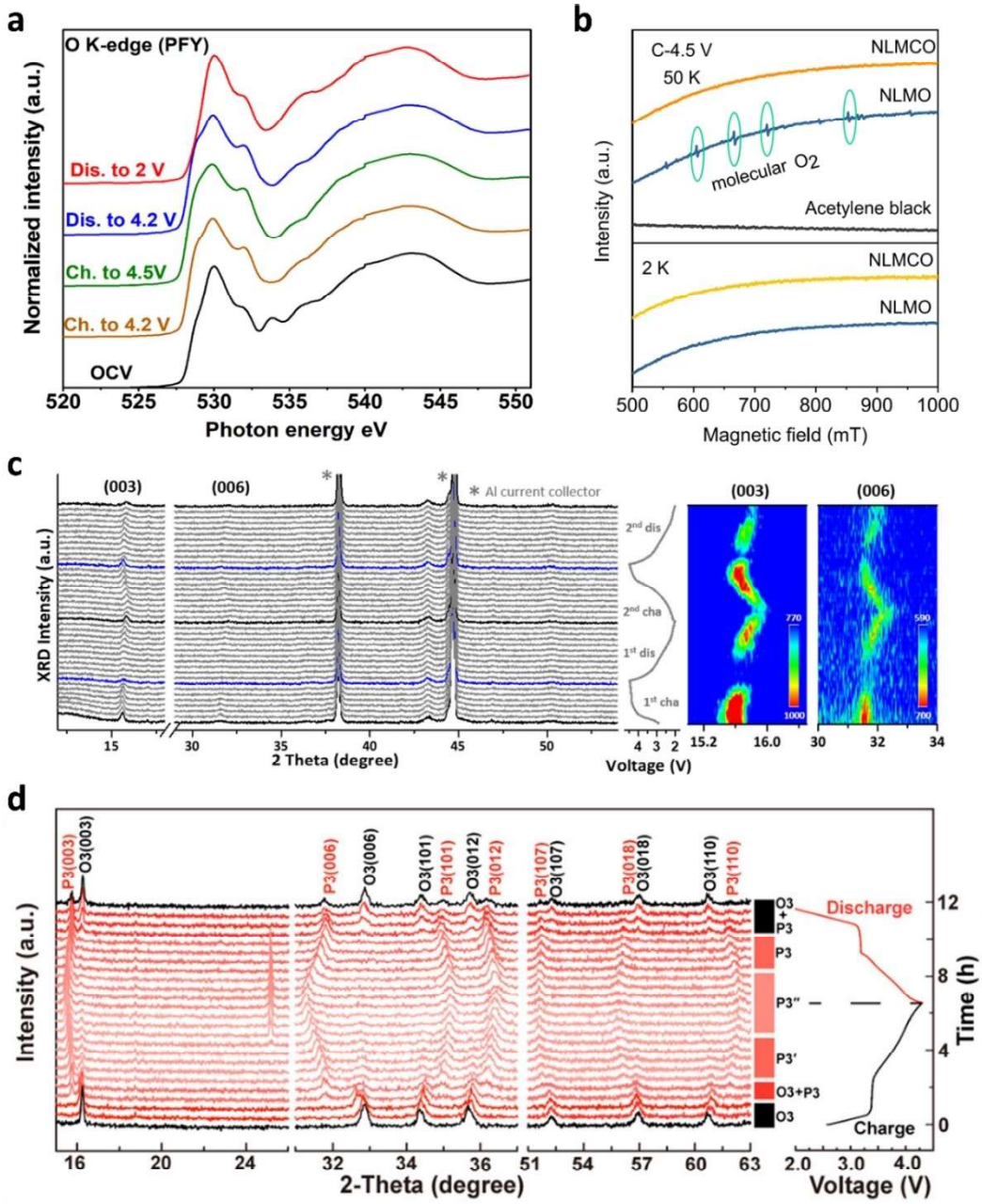

Figure 3. a) O K-edge XAS spectra of P2–$Na_{0.78}Co_{1/2}Mn_{1/3}Ni_{1/6}O_2$. Reproduced with permission from Ref. [47]. Copyright (2020) Nature. b) *Ex-situ* X-band EPR spectra of P2–$Na_{0.73}Li_{0.21}Mn_{0.74}Cu_{0.05}O_2$ under 2 K and 50 K. Reproduced with permission from Ref. [50]. Copyright (2022) American Chemical Society. c) *Ex-situ* XRD patterns of P3-$Na_{0.5}Mg_{0.15}Al_{0.2}Mn_{0.65}O_2$. Reproduced with permission from Ref. [117]. Copyright (2021) American Chemical Society. d) *In-situ* XRD patterns of O3–$Na0_{.8}Ni_{0.6}Sb_{0.4}O_2$. Reproduced with permission from Ref. [58]. Copyright (2021) American Chemical Society.

O3–$Na[Ni_{4/9}Mn_{1/3}Mg_{1/18}Ti_{1/6}]O_2$ which was co-doped with electrochemically inactive element Mg^{2+} and highly oxidized element Ti^{4+}.[55] The structure delivered a large discharge capacity of ~198 mAh g^{-1} at 12 mA g^{-1} and maintained ~70% of the initial capacity after 50 cycles at 12 mA g^{-1}. Compared with the non-doped pristine sample, O3–$Na[Ni_{4/9}Mn_{1/3}Mg_{1/18}Ti_{1/6}]O_2$ was confirmed to alleviate the structural change with slab shrinkage via the formation of additional OP2-like interphase during the O3–P3 phase transition near 4.2 V.

3.2. Polyanion compounds

NASICON (Na-super ionic conductor) materials are the most well-known polyanionic cathode materials for NIBs; nevertheless, various studies on polyanion cathode materials with numerous crystal structures have been performed. This type of cathode material possesses not only a high redox potential but also outstanding structural stability and is thus suitable for NIBs with alkali-metal ions of larger ionic radius. Recently, fluorophosphate-based materials have received great attention because additional redox potentials could be accessed.[121,122]

Meanwhile, the design of carbon composites to improve electrical conductivity has received considerable attention to improve the electrochemical performance of polyanion-based cathodes. The formation of composites with conductive carbon such as acetylene black, single- and multi-walled carbon nanotubes (CNTs) and graphene, and the fabrication of nano-structures using high-energy ball-milling or spray-drying have been attempted to improve the electrochemical performance of polyanion compound.

The $Na_3V_2(PO_4)_3$, a representative material of NASICON, is attracting attention for its excellent Na ion conductivity and high operating voltage.[31,123] Nevertheless, its inherently low conductivity requires an additional conductive carbon coating, resulting in lower gravitational energy density. Li at el. studied Mg-doped $Na_{3.05}V_{1.95}Mg_{0.05}(PO_4)_3$ to enhance the electrochemical properties of $Na_3V_2(PO_4)_3$.[124] In the range of 2.5–4.0 V, it delivered 102 mAh g^{-1} at a current rate of 1 C (117 mA g^{-1}), and maintained ~92 mAh g^{-1} at 20 C (2340 mA g^{-1}), indicating an excellent rate-capability by Mg doping (Figure 4a). It is revealed that more Na^+ is introduced to maintain the charge balance, as Mg element is doped into the $Na_3V_2(PO_4)_3$ crystal structure. In addition, comparison of the first-principles calculation and

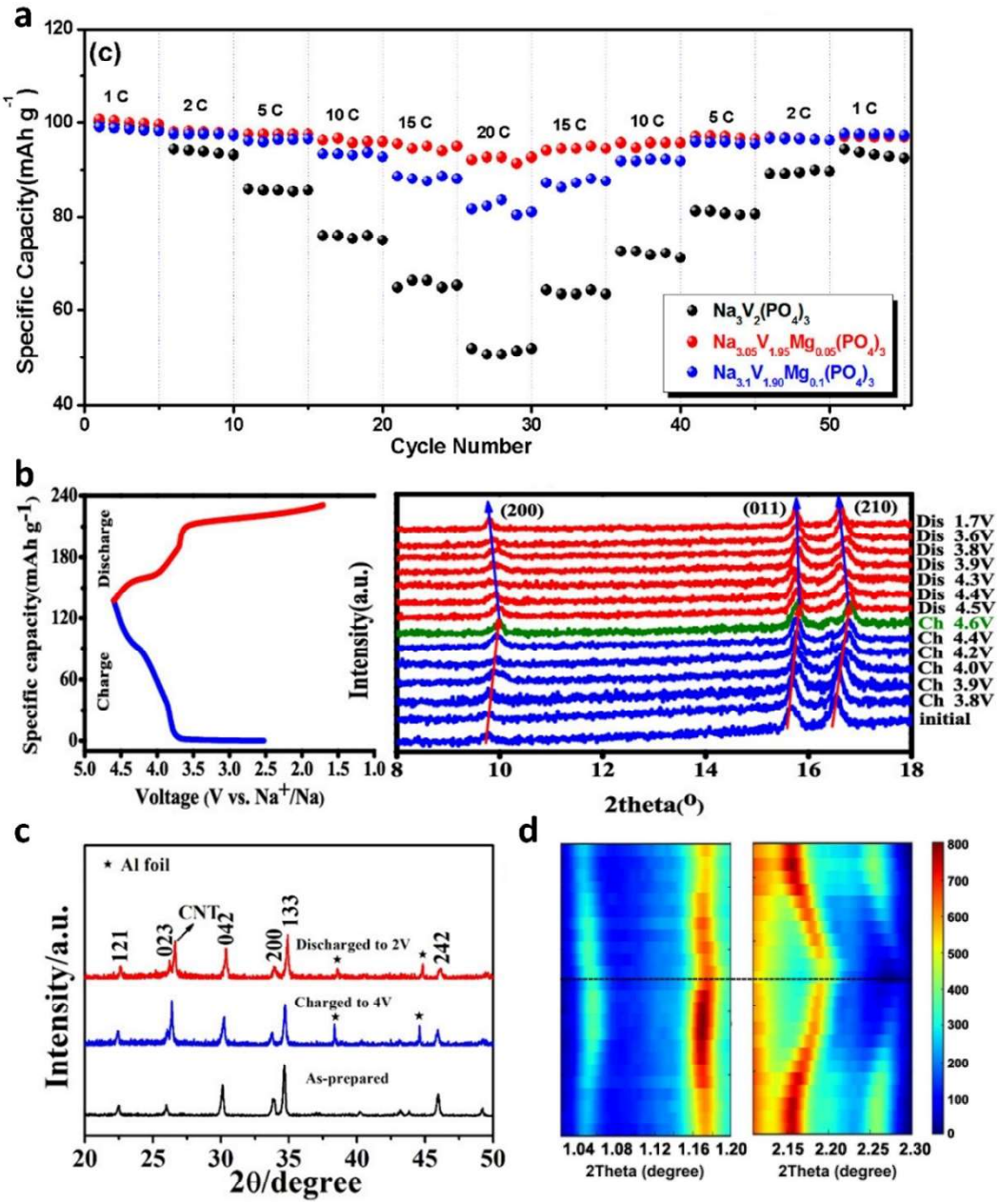

Figure 4. a) Rate-capability of $Na_{3+x}V_{2-x}Mg_x(PO_4)_3/C$ ($x=0$, 0.05, and 0.1). Reproduced with permission from Ref. [124]. Copyright (2018) American Chemical Society. b) *Ex-situ* XRD patterns of $Na_4Mn_2Co(PO_4)_2P_2O_7$. Reproduced with permission from Ref. [68]. Copyright (2019) American Chemical Society. c) *Ex-situ* XRD patterns of Na_2FePO_4F. Reproduced with permission from Ref. [62]. Copyright (2020) American Chemical Society. d) *In-situ* XRD patterns of $Na_{2.4}Fe_{1.8}(SO_4)_3$. Reproduced with permission from Ref. [72]. Copyright (2020) Elsevier.

Rietveld calculation result indicated that the Mg dopant was not uniformly distributed in the material, with electrochemical impedance spectroscopy (EIS) analyses confirming this suggestion. The size of the semicircle in the Nyquist plot decreased as the temperature increased, corresponding to a decrease of the interphase resistance. Considering that the un-doped sample hardly changes the interfacial resistance with temperature, the Mg dopant is mainly distributed on the surface of the cathode material and affects the electrochemical performance of the cathode material.

In the case of Mn-based polyanion structures, it is reported that the use of two or more transition metals improves overall electrochemical performances by suppressing the Jahn-Teller distortion effect of Mn^{3+}.[125,126] Tang et al. reported on a mixed-polyanion $Na_4Mn_2Co(PO_4)_2P_2O_7$ composite with improved operating voltage and cycle performance.[68] In the range of 1.7–4.6 V, $Na_4Mn_2Co(PO_4)_2P_2O_7$ modified with CNTs delivered a capacity of ~96.1 mAh g^{-1} at 0.1 C (~12.8 mA g^{-1}), and it retained ~76.4% of the initial capacity measured at 1 C (~128 mA g^{-1}) after 150 cycles. *Ex-situ* XRD was performed to verify the structural stability of $Na_4Mn_2Co(PO_4)_2P_2O_7$ (Figure 4b). During the charge process, the (200), (011) and (210) peaks gradually shifted toward higher angle, indicating the decrease in lattice parameters by Na^+ deintercalation. After the discharge process, each peak is restored its original position, confirming that reversible structural change occurred during the charge and discharge process.

Xun et al. reported on a fluorophosphate-based Na_2FePO_4F composite fabricated via hydrothermal synthesis and ball milling with conductive carbon.[62] With the high electronegativity of fluorine in crystal structure, it exhibited a high working voltage of ~3.0 V. The composite delivered a capacity of 118 mAh g^{-1} at 0.1 C (~12.4 mA g^{-1}) in the range of 2.0–4.0 V. After 2500 cycles, it maintained ~58% of the initial capacity at 5 C (~620 mA g^{-1}). The structural stability of Na_2FePO_4F was verified by *ex-situ* XRD (Figure 4c). Each peak shifted negligibly during cycling, thus its crystal structure was well retained during the 1 mol Na^+ de/intercalation.

Various studies on non-stoichiometric polyanion cathode materials have been conducted to enhance electrochemical properties.[32,127–129] Additional capacity could be obtained through excess Na^+ ions in the crystal structure replacing the transition metal, and structural stability is also improved by the presence of residual Na^+ ions in crystal structure during the Na^+ de/intercalation. Fang at el. studied the sulfate-based polyanion compound $Na_{2.4}Fe_{1.8}(SO_4)_3$.[72] To improve the low conductivity of the cathode material, spray drying with low-temperature heat treatment was introduced to form a microsphere covered by reduced graphene oxide (rGO). In the range of 2.0–4.4 V, it delivered a capacity of 100 mAh g^{-1} at 0.05 C (~5 mA g^{-1}), corresponding to 100% of the theoretical capacity. In addition, the compound delivered specific capacity of 45 mAh g^{-1} at a high current rate of 50 C (~5000 mA g^{-1}). A cyclability test was performed at 10 C (1000 mA g^{-1}) during 10000 cycles, and $Na_{2.4}Fe_{1.8}(SO_4)_3$ retained ~58% of the initial capacity. *In-situ* synchrotron XRD was performed to investigate the structural change (Figure 4d). In the magnified XRD plot, (020), (200), ($\bar{1}$12) and ($\bar{3}$12) peaks appeared in a series order from the left. During the charge process, the (200) peak shifted to the lower angle, while the other peaks shifted to the high angle. Reversible structural changes were observed during cycling, with the changes along the *a*-axis and *b*-axis of 0.8%, respectively, which is related to the negligible volume expansion of ~0.4%.

3.3. Prussian blue analogues

Prussian blue analogues have been widely studied over the past 10 years owing to their robust crystal structure and sufficient space for large alkali ions. Although their use as a cathode in non-aqueous LIB systems was attempted, poorer electrochemical properties were observed, originating from the relatively small size of the Li^+ ions compared with the interstitial sites.[36,130] Generally, Prussian blue analogue cathodes for NIBs have the advantage of a larger theoretical capacity (~170 mAh g^{-1}) than for KIBs (~150 mAh g^{-1}); however, their theoretical electrochemical performance could not be attained due to the higher content of crystalline water.[131] Therefore, many recent works have focused on the achieving theoretical capacity of Prussian blue analogues for NIBs by enhancing the crystallinity via the assistance of a chelating agent or surfactant. In addition, substitution of N-coordinated high-spin transition metal with other transition metal has also been attempted to enhance the electrochemical performance.

Element doping is one of the effective way to improve the structural stability for Prussian blue cathode, suppressing the formation of defects and crystalline water in the crystal structure.[78,132,133] Chen et al. introduced the Cu dopant effect for Fe-based Prussian blue analogues.[73] Cu-doped $Na_{1.68}Fe_{0.92}Cu_{0.08}[Fe(CN)_6]_{0.86}\square_{0.14}\cdot 1.43H_2O$ (Cu–FeHCF) was observed to have greater Na^+ content and lower vacancy content than the pristine sample through various analyses, and the uniform Cu doping was confirmed by X-ray photoelectron spectroscopy (XPS) measurement with Ar-ion sputtering. The Cu dopant effect was measured by electrochemical test in the range of 2.0–4.3 V at a current rate of 100 mA g^{-1} (Figure 5a). During the initial 3 cycles, Cu–FeHCF delivered 127, 123 and 122 mAh g^{-1} of discharge capacity, while the undoped FeHCF samples showed inferior electrochemical performance. This additional capacity is originated to wider voltage plateau in the high voltage region, which related to the activation of low-spin Fe elements. In addition, Cu–FeHCF exhibited long cycle performance, retaining ~76% of the initial capacity after 500 cycles measured at 5000 mA g^{-1}. Furthermore, the low interphase resistance and high Na^+ diffusion coefficients due to the Cu dopant effect were verified by EIS analyses and galvanostatic intermittent titration technique (GITT) measurement, respectively.

Recently, rhombohedral-phase Prussian blue analogues have been attracting attention due to their high electrochemical performance derived from high Na^+ content with low water content.[134–136] Xie et al. reported the structural change of Ni-based rhombohedral Prussian blue analogue cathode during

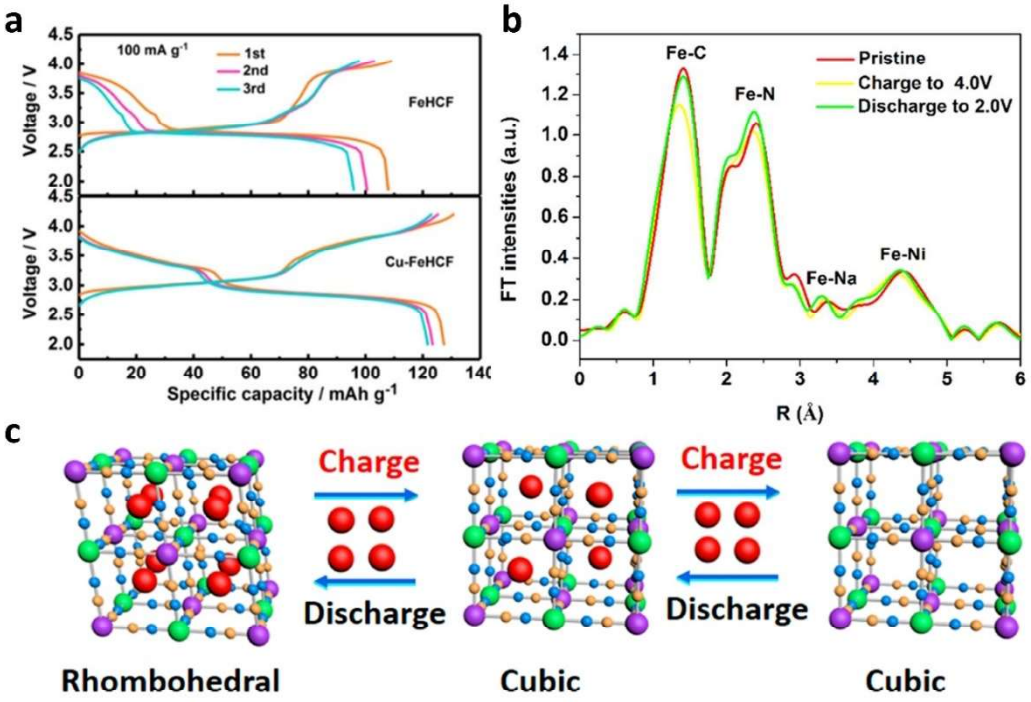

Figure 5. a) Initial three voltage profiles of FeHCF and Cu–FeHCF. Reproduced with permission from Ref. [73]. Copyright (2022) American Chemical Society. b) *Ex-situ* XRD patterns of $Na_{1.34}Ni[Fe(CN)_6]_{0.81}$. Reproduced with permission from Ref. [74]. Copyright (2019) American Chemical Society. c) Fe K-edge XANES spectra of $Na_{1.34}Ni[Fe(CN)_6]_{0.81}$. c) Schematic illustration of $Na_2Fe_4[Fe(CN)_6]_3$ for phase transition. Reproduced with permission from Ref. [78]. Copyright (2021) American Chemical Society.

Na^+ de/intercalation.[74] In the range of 2.0–4.0 V, rhombohedral $Na_{1.34}Ni[Fe(CN)_6]_{0.81}$ delivered 68 mAh g^{-1} at 0.2 C (17 mA g^{-1}), and 87.8% of the initial capacity was maintained after 10000 cycles at 10 C (850 mA g^{-1}). Compared to cubic phase, the rhombohedral phase exhibited improved electrochemical performance, which is originated to low defect in crystal structure. *Ex-situ* XRD revealed that it undergoes a rhombohedral-cubic phase transition, accompanied by peak splitting with small lattice distortion. During the Na^+ de/intercalation, the reversible Fe^{2+}/Fe^{3+} redox reaction was observed through X-ray absorption near edge structure (XANES) analyses, whereas electrochemically inactive Ni^{2+} contributed to structural stability by mitigating the volume change due to Na^+ migration along with the phase transition. In addition, extended X-ray absorption fine structure (EXAFS) analyses revealed that the asymmetrical shape of the Fe–N bond peak was alleviated in the charged state, which is related to the local structural distortion caused by phase transition (Figure 5b). In particular, the Fe–Na bond distance was shorter in the discharge state than pristine state, which indicates that more Na^+ intercalation occurred by the reduction of Fe^{3+}.

Qin et al. studied the high-crystalline Prussian blue analogue $Na_2Fe_4[Fe(CN)_6]_3$ to enhance the overall electrochemical properties.[78] Compared to conventional co-precipitation method, highly crystalline $Na_2Fe_4[Fe(CN)_6]_3$ with low defects or water content was synthesized by controlling the concentration of citric acid. It delivered specific capacity of ~120 mAh g^{-1} at 2 C (240 mA g^{-1}), whereas the conventional low-crystalline sample only delivered a capacity of 60 mAh g^{-1} with low redox potential. The high crystallinity of the Prussian blue analogue also affected the rate-capability, with a discharge capacity of 78 mAh g^{-1} maintained even at the high current density of 100 C (12000 mA g^{-1}). In addition, 62% of initial capacity was maintained after 2000 cycles measured at high current rate of 10 C (1200 mA g^{-1}). *In-situ* XRD results revealed that high-crystalline $Na_2Fe_4[Fe(CN)_6]_3$ could accommodate up to 4 mol of Na^+ ions per formula unit with reversible rhombohedral-cubic phase transition, in contrast to the low-crystalline sample, which could accommodate up to 2 mol of Na^+ ion without the rhombohedral phase transition (Figure 5c). It was considered that defects and coordinated water molecules in lattice structure reduce the Na^+ active sites, inhibiting efficient energy storage as well as rapid ion diffusion.

4. Cathode Materials for K-Ion Batteries

4.1. Layered oxides

The larger ionic radius of the K^+ ion limits the selection of appropriate crystal structures in the KIB system. Most layered oxide cathode materials possess the P-type structure owing to the strong K^+–K^+ repulsion, with only a few layered oxides with the O-type structure, such as O3–$KCrO_2$.[90] As layered oxide cathodes for KIBs usually undergo severe structural distortion, many studies have focused on how to mitigate these structural changes. In particular, since the Mn-based layered cathode have been highly preferred in KIB system owing to its

high capacity with low-cost advantages, these studies were mainly focused on suppressing the Jahn-Teller distortion of Mn^{3+} by substitution with other transition metals, such as nickel, cobalt and iron.

Zhang et al. demonstrated Ni/Mn-based P2–$K_{0.44}Ni_{0.22}Mn_{0.78}O_2$.[79] In the range of 1.5–4.0 V, it delivered a discharge capacity of 121 mAh g^{-1} at 10 mA g^{-1}, and a capacity of 58 mAh g^{-1} was achieved at the high current rate of 500 mA g^{-1}. After 500 cycles, P2–$K_{0.44}Ni_{0.22}Mn_{0.78}O_2$ retained 67% of the initial capacity at a current rate of 200 mA g^{-1}. It was thought that this high-cyclability is due to the small structural changing of P2–$K_{0.44}Ni_{0.22}Mn_{0.78}O_2$, which is shown in *in-situ* XRD result (Figure 6a). During the charge process, the (002) and (004) peaks shifted toward low angle while (010) and (012) peaks shifted toward higher angle, indicating decrease of a and b lattice parameters with increase of c lattice parameter. As a result, the difference of the volume between full-charged state and full-discharged state was only ~1.5%. Meanwhile, it showed reversible structural change and maintained P2 phase without the phase transition during the cycling.

Many studies have been reported on the correlation of electrochemical performance according to the arrangement of transition metal layers for layered-type cathode materials. In particular, the honeycomb structural framework combined with

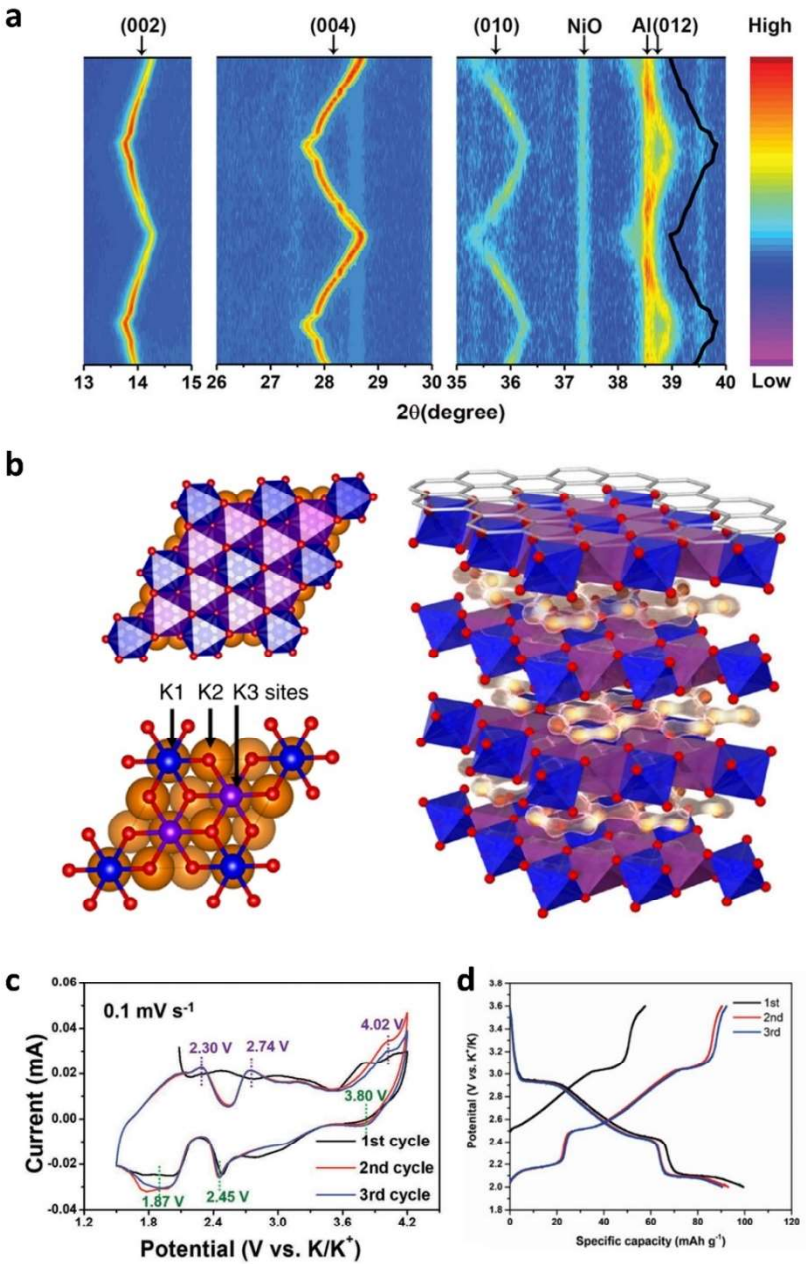

Figure 6. a) *In-situ* XRD patterns of P2–$K_{0.44}Ni_{0.22}Mn_{0.78}O_2$. Reproduced with permission from Ref. [79]. Copyright (2022) Wiley-VCH. b) Structural images with bond-valence energy landscape map of P2–$K_2Ni_2TeO_6$. Reproduced with permission from Ref. [81]. Copyright (2018) Nature. c) Cyclic voltammetry profile of P2–$K_{0.65}Fe_{0.5}Mn_{0.5}O_2$. Reproduced with permission from Ref. [80]. Copyright (2018) Wiley-VCH. d) Voltage profile of P'3–$K_{0.3}Mn_{0.95}Co_{0.05}O_2$. Reproduced with permission from Ref. [139]. Copyright (2019) Wiley-VCH.

highly oxidized M element (M=As, Sb, Te, *etc.*) effectively improves structural stability, leading to higher energy density and better cycling stability.[137,138] Masese at el. reported on Ni/Te-based P2–$K_{2/3}Ni_{2/3}Te_{1/3}O_2$, which exhibited honeycomb ordering of the transition metals.[81] Through the Rietveld refinement, it has honeycomb structure in which each TeO_6 octahedra is surrounded by NiO_6 octahedra in the transition metal layer (Figure 6b). P2–$K_2Ni_2TeO_6$ has distinguishable three K atom sites (K1, K2 and K3), and all K sites are consisted prismatic coordination; However, these K sites are only partially occupied, suggesting the disordered distribution of K^+ ions between the transition metal layers and the possibility of additional K^+ ion intercalation. In addition, the bond-valence energy landscape (BVEL) analysis was performed to predict the possible ionic diffusion pathways and atomic sites for K^+ ions, which revealed the two-dimensional diffusion pathways and a low activation barrier energy compared with not only the cathode material but also the solid electrolyte. Further analysis of its high ionic conductivity was performed by first-principles calculation. The density of states (DOS) revealed that the band gap was significantly reduced after the K^+ deintercalation, implying the facile ionic diffusion of P2–$K_2Ni_2TeO_6$. Unlike the electrochemically inactive Te element, Ni and O showed a high degree of hybridization, which is related to the charge-compensation mechanism during the K^+ de/intercalation.

Deng et al. reported on P2–$K_{0.65}Fe_{0.5}Mn_{0.5}O_2$ microsphere as a cathode material for KIB, which used low-cost and earth-abundant transition metals.[80] Synthesis of microsphere particles was introduced to not only improve the sluggish kinetics of K^+ de/intercalation, but also reduce the side reaction with electrolyte. The cyclic voltammetry (CV) test was performed to verify the cathodic and anodic electrochemical reaction in the range of 1.5–4.2 V with scan rate of 0.1 mV s^{-1}, as shown in Figure 6(c). The two redox pairs in the low-voltage region (2.30 and 1.87 V, 2.74 and 2.45 V) and one redox pair in the high-voltage region (4.02 and 3.80 V) were observed, indicating the Mn^{3+}/Mn^{4+} and Fe^{3+}/Fe^{4+} redox couple, respectively. In galvanostatic charge/discharge tests, it delivered a capacity of 151 mAh g^{-1} at 20 mA g^{-1}, and it retained 78% of the initial capacity after 350 cycles at 100 mA g^{-1}. Compared to cathode material synthesized by conventional solid-state method, P2–$K_{0.65}Fe_{0.5}Mn_{0.5}O_2$ has numerous pores in the microsphere, which is efficiently suppressed the excessive volume change to enable the long-term cycle.

Zhang at el. studied the Co-doped effect of P′3–$K_{0.3}Mn_{0.95}Co_{0.05}O_2$.[139] Only 5% cobalt was doped to replace manganese, but the redox behavior differed significantly compared with that of the pristine $K_{0.3}MnO_2$, including low polarization and a distinct redox-pair. Moreover, the Jahn-Teller distortion of Mn^{3+} was successfully suppressed, because activation of the Co^{4+}/Co^{3+} redox couple reduces the total amount of Mn^{3+}, leading to more stable electrochemical properties. In the range of 2.0–3.6 V, the initial discharge capacity of P′3–$K_{0.3}Mn_{0.95}Co_{0.05}O_2$ was 99 mAh g^{-1} at a current rate of 22 mA g^{-1}, whereas that of pristine P′3–$K_{0.3}MnO_2$ was only 77 mAh g^{-1} at the same current rate (Figure 6d). Interestingly, the additional capacity mainly attributed to low voltage region, suggesting that the mitigation of structural distortion also affects the capacity improvement. In addition, at a current rate of 440 mA g^{-1}, 55% of the discharge capacity measured at 22 mA g^{-1} was retained, indicating the improved rate-capability compared to the 36% retention of pristine sample. These findings suggest that small amounts of Co dopant could effectively suppress the Jahn-Teller distortion of Mn^{3+} to improve the overall electrochemical performance.

4.2. Polyanion compounds

Polyanion cathode materials are more suitable for KIB systems that require a robust structural framework and high operating voltage. Moreover, polyanion cathode materials can effectively weaken the K^+–K^+ interaction originated from large ionic radius, storing ions in sufficiently large three-dimensional space.[109] In particular, fluorophosphate-based cathode materials for high operating voltage are attracting attention, similar to polyanion cathode materials for NIBs. On the other hands, the formation of conductive carbon composite is highly required to solve the inherent problem of electrical conductivity and suppress the volume expansion during cycling.

Fedotov at el. reported on the Ti-based fluorophosphate cathode material $KTiPO_4F$.[96] Since the phosphate-based materials have low electronic conductivity, they conducted carbon coating using a solution of polyvinyl cyanide with a 4–5 nm thickness on the surface of round-shape $KTiPO_4F$ particles uniformly. In the range of 2.0–4.2 V, it delivered a capacity of 94 mAh g^{-1} at C/20 (6.65 mA g^{-1}) with distinguishable voltage plateaus. In addition, it maintained 97% of the initial capacity after 100 cycles at the high current rate of 2 C (266 mA g^{-1}). The structural change of $KTiPO_4F$ was verified by *operando* synchrotron XRD, and reversible redox reaction involving multiple two-phase transitions was observed during cycling (⁻). During K^+ deintercalation, the compound underwent two-phase transition from orthorhombic (*P n a* 2_1; 2.0–2.9 V and 3.1–3.4 V) to monoclinic (*C m*; 2.9–3.1 V) and another orthorhombic structure (*P n a n*; 3.4–4.2 V); however, the total cell volume change was ~6.5%, indicating the excellent structural stability of $KTiPO_4F$.

Bodart et al. synthesized $K_3V(PO_4)_2$/C composites using the spray-drying method.[97] In this research, they conducted two solutions to enhance the electrochemical properties of the $K_3V(PO_4)_2$; The low electronic conductivity of polyanion cathode material was improved by preparing composite material with various carbon sources such as CNT and rGO. In addition, additional ball-milling process was performed to increase the surface area of the composite material and shorten the ion diffusion path. After the milling process, the electrochemical tests were performed in the range of 2.0–4.5 V. The specific discharge capacity of $K_3V(PO_4)_2$/CNT composite was increased to 101 mAh g^{-1} at a current density of C/20 (7.5 mA g^{-1}). However, in case of composite containing rGO, the discharge capacity was noticeably decreased. EIS analyses were further performed to confirm the low electrochemical performance of the sample containing rGO. As shown in Figure 7(b), it was confirmed that the interface resistance after ball-milling

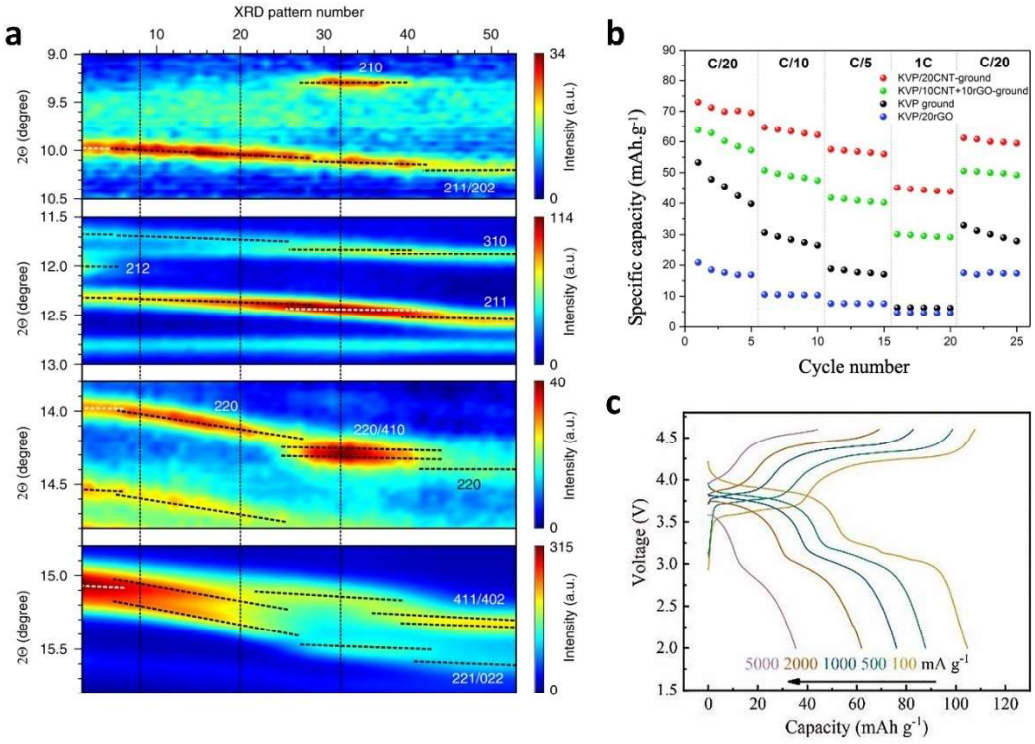

Figure 7. a) *Operando synchrotron* XRD patterns of $KTiPO_4F$. Reproduced with permission from Ref. [96]. Copyright (2020) Nature. b) Rate-capability of $K_3V(PO_4)_2$ for different coating sources. Reproduced with permission from Ref. [97]. Copyright (2020) Elsevier. c) Voltage profile of $Na_3V_2O_2(PO_4)_2F$ at different current densities. Reproduced with permission from Ref. [98]. Copyright (2022) Elsevier.

significantly increased, indicating that the rGO structure was destroyed during the ball-milling process and thus did not play the role of conductive carbon.

Due to the difficulty of direct synthesis, a number of studies have been reported using indirect synthesis methods such as ion-exchange process.[93,99] Zhang et al. studied $K_3V_2O_2(PO_4)_2F$ prepared through the Na^+/K^+ ion-exchange process.[98] Based on the $Na_3V_2O_2(PO_4)_2F$, Na^+/K^+ ion-exchange was proceeded under K-ion battery system using K metal anode for 30 cycles. High electrochemical properties were realized in the KIB system by reducing the particle size without carbon coating. The crystal structure was well maintained even after 30-cycled ion-exchange, except for changes in the lattice parameters due to the larger radius of K^+ ions. The compound delivered a discharge capacity of 105 mAh g^{-1} at 100 mA g^{-1} in the range of 2.0–4.6 V, and it retained a capacity of 35 mAh g^{-1} even at the high current rate of 5000 mA g^{-1} (Figure 7c). It is considered that the fluorophosphate-based open framework with high electronegativity of F^- enables the high operating voltage and facile diffusion of K^+.[140,141] In cycle tests, $K_3V_2O_2(PO_4)_2F$ showed good cyclability, with capacity retention of 87% after 200 cycles at 100 mA g^{-1}.

4.3. Prussian blue analogues

With preference for the large K^+ ions, many researchers focused on Prussian blue analogue cathode materials for KIBs. A high working voltage with large discharge capacity were achieved in the monoclinic or rhombohedral phase as well as the cubic phase. In addition, approaches for aqueous electrolyte batteries have been attempted due to the safety advantage and small hydrated ionic radius of K^+.[37,142] Recently, despite the electrochemical inertness of nickel element, various approaches have been attempted to replace N-coordinated high-spin transition metal with nickel to improve structural stability with power-capability of Prussian blue analogue cathode materials in KIB system.

Chong et al. reported on the changes in the electrochemical performance upon the substitution of N-coordinated transition metals.[103] In this experiment, some of the N-coordinated high-spin Fe elements were substituted with Ni elements, and the half-substituted $K_{1.90}Ni_{0.5}Fe_{0.5}[Fe(CN)_6]_{0.89}$ (KNFHCF-1/2) showed significantly low water contents (10.87% of adsorbed water and 2.31% of interstitial water) than bare sample contents (17.58% of adsorbed water and 2.73% of interstitial water) (Figure 8a). Through additional analyses such as ICP-AES and elemental analyses, it was found that the Ni substitution suppressed the formation of defects and crystalline water in lattice structure. In the range of 2.0–4.5 V, it delivered a capacity of 81.6 mAh g^{-1} at 10 mA g^{-1}; However, this capacity was lower than that of the bare sample (116.8 mAh g^{-1}), due to the electrochemical inertness of the substituted Ni element. Nevertheless, the rate-capability and cyclability of significantly improved. The KNFHCF-1/2 delivered 53.4 mAh g^{-1} at a high current density of 500 mA g^{-1}, which retained 66% of capacity

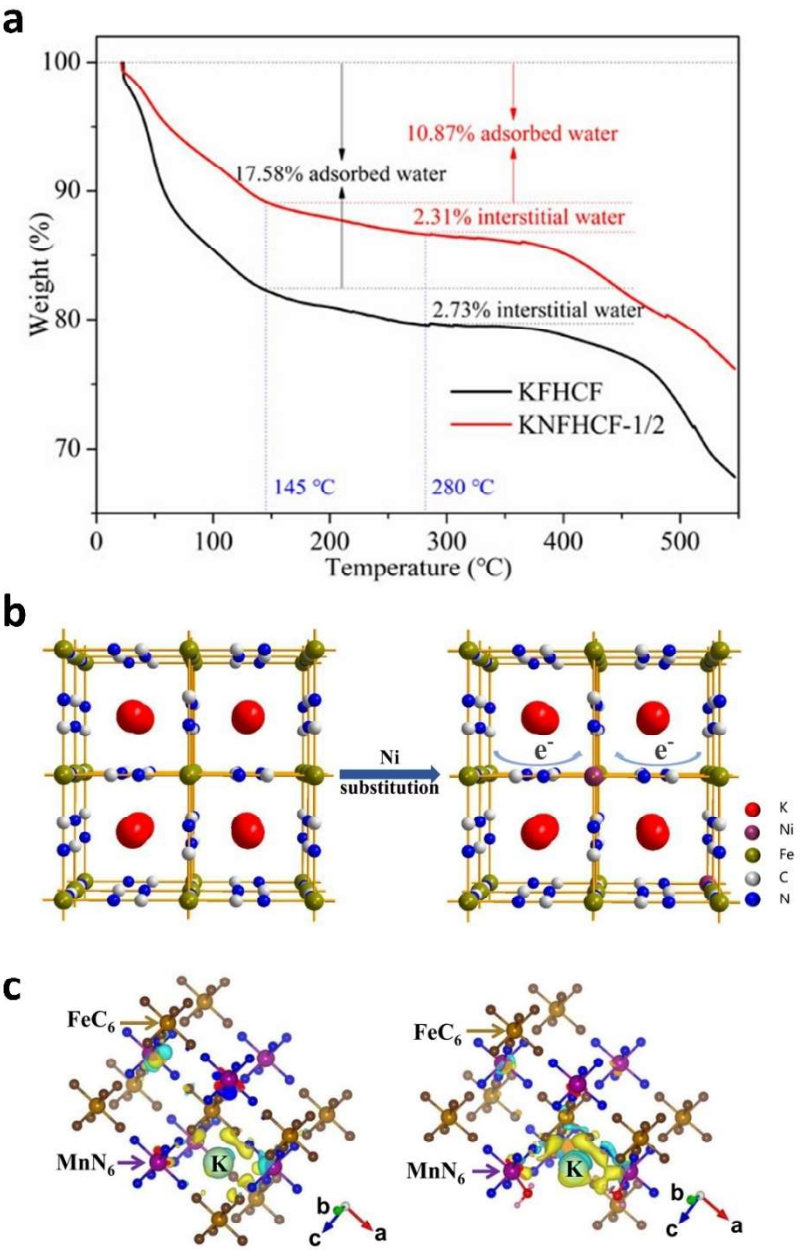

Figure 8. a) Thermogravimetric analysis curves of KFHCF and KNFHCF-1/2. Reproduced with permission from Ref. [103]. Copyright (2020) American Chemical Society. b) Schematic illustration of $K_2Ni_xFe_{1-x}[Fe(CN)_6]$ for Ni dopant effect. Reproduced with permission from Ref. [104]. Copyright (2019) American Chemical Society. c) Visualized charge density of $K_2Mn[Fe(CN)_6]$ according to the defect. Reproduced with permission from Ref. [106]. Copyright (2021) Nature.

measured at 20 mA g^{-1}. In the long-term cycle test, KNFHCF-1/2 retained 82.3% of the initial capacity after 1000 cycles at 100 mA g^{-1}. The DOS revealed that Ni substitution activated the C-coordinated low-spin Fe^{2+}/Fe^{3+} redox reaction, although Ni element did not directly contribute to the capacity.

Huang et al. studied the effect of Ni dopant to optimize the electrochemical performance of iron hexacyanoferrate ($K_2Ni_xFe_{1-x}[Fe(CN)_6]$, $x = 0$–0.08).[104] Through XRD analyses, it was observed that the full width at half-maximum (FWHM) of the peak widened as the dopant concentration increased from 0 to 0.08 mol, indicating a decrease in the particle size. In addition, the average lattice size was also decreased as the content of Ni dopant increased. Electrochemical tests were conducted in the range of 2.0–4.5 V, and all the samples showed an identical redox pair around 3.1/3.6 V and 3.7/4.1 V. Among them, the optimized sample of $K_{1.63}Ni_{0.05}Fe_{0.95}[Fe(CN)_6]$ delivered highest capacity of ~124 mAh g^{-1} at 50 mA g^{-1} than others, and it retained a discharge capacity of 81 mAh g^{-1} even at 400 mA g^{-1}. They claimed that Ni dopant replaced the N-coordinated high-spin Fe element, and the binding energy of N 1s is increased due to the higher electronegativity of Ni^{2+} (1.91) than Fe^{2+} (1.88). As a result, the electron atmosphere of the C-coordinated low-spin Fe was affected, thereby reducing the binding energy of Fe $2p_{3/2}$ and raising the Fe^{2+}/Fe^{3+} redox potential (Figure 8b).

Deng at el. introduced the $K_2Mn[Fe(CN)_6]$, which has a low content of defects and water, through the co-precipitation method with ethylenediaminetetraacetic acid dipotassium salt (EDTA-2 K) as the chelating agent.[106] During the co-precipitation reaction, $[Mn(EDTA)]^{2-}$ slowly releases Mn^{2+} to slow the nucleation and growth, greatly inhibiting the formation of defects and crystalline water in the lattice structure. In the range of 2.7–4.4 V, $K_2Mn[Fe(CN)_6]$ delivered a capacity of 136.7 mAh g^{-1} at 30 mA g^{-1}, and it retained a discharge capacity of 74 mAh g^{-1} at 500 mA g^{-1}. In addition, it maintained 69% of the initial capacity after 10000 cycles at the high current density of 500 mA g^{-1}. The defect-free effect was verified through first-principles calculations. The predicted redox potential of the non-defective sample (3.9 V and 3.3 V) was much higher than that of the defective sample (3.0 V and 2.88 V), suggesting that the defects in the crystal structure result in deterioration of the electrochemical properties. In addition, the activation barrier energy for K^+ migration was increased by the presence of lattice defects, from 0.53 eV to 0.65 eV. The visualization of charge density shows that these defect causes the strong interaction to K^+ ion, resulting in high activation barrier energy for K^+ diffusion (Figure 8c).

5. Conclusion and Perspective

Since the 2010s, the demand for more economical energy storage devices has surged due to the rapid rise in raw material prices, and NIBs and KIBs are attracting attention as potential candidates to replace LIBs. Compared with other candidates, these materials have many advantages such as abundant raw materials for the alkali metal with low price, and an electrochemical reaction similar to that of LIBs. In this review, we aimed to compare the two battery systems from a broad perspective, and outline possible research directions as an alternative to LIBs. Therefore, structure of cathode materials is classified into three major categories, and pros and cons of different cathode materials are comparatively discussed. Meanwhile, the improvement direction of the cathode material is also suggested by considering the electrochemical characteristics, structural deformation, and local structural changes according to classified structure type. Although remarkable progress has been achieved in the past decades, several challenges remain for improvement to realize high-performance next-generation secondary batteries. First, the selection of inexpensive transition metals has become inevitable as the price of rare-earth raw materials continues to rise. Cobalt and nickel are used for high-performance cathode materials for LIBs; however, these choices are not suitable for economical energy-storage design. For example, the prices of cobalt and nickel were ~30,000 and ~12,000 USD/ton in 2019, but these prices have soared to ~51,000 and ~22,000 USD/ton in 2022, respectively. Meanwhile, the prices of manganese and iron were ~1,300 USD/ton and ~90 USD/ton in both 2019 and 2022.[13] Thus, intensive studies based on earth-abundant transition metals, such as iron and manganese, are required to realize competitive next-generation energy-storage devices. Second, it is necessary to study cathode materials in consideration of excessive volume change and complex ion diffusion mechanism, due to the larger ionic radius with consequent structural degradation. This issue is particularly highlighted in layered oxide materials, where strong repulsion between the alkali ions and ion/vacancy ordering occur. To address this issue, the introduction of electrochemically inactive elements such as Mg and Al may be necessary as one method for structural stabilization. Third, for practical use of NIB and KIB cathode materials, studies on chemical instability upon air exposure as well as moisture intercalation should be addressed. NCM, a state-of-the-art layered oxide cathode material widely used in LIBs, also suffers from this problem, resulting in the formation of LiOH or Li_2CO_3 and consequent irreversible lithium loss.[143,144] In NIB and KIB systems, electrically insulating materials could be formed on the surface of the cathode material through a similar mechanism, which interfere with normal reaction and degrade the overall electrochemical performance. The application of an air-stable coating layer on the surface is an effective way to prevent these side reactions; however, the reduction in the gravimetric energy density and the additional cost of the coating process must be considered. Fourth, an alternative to alkali-ion deficiency or the ion-exchange process is required for the commercialization of NIBs and KIBs. To compensate for the problem of ion deficiency of the cathode, various methods such as presodiation/prepotassiation of the anode and the use of a sacrificial salt have been proposed.

Although both NIB and KIB use alkali ions as charge carriers, but the different ionic radius brings in huge differences in electrochemical properties with structural changes. Therefore, it is important to select an appropriate cathode material structure for each battery system. In case of NIBs, despite the high redox potential of Na/Na^+, various studied for layered oxide cathode have reported their high energy densities over 600 Wh kg^{-1}, not only P-type structures but also O-type structures.[54,55,59] However, these materials undergo severe volume expansion with phase transition (P2-OP4-O2, O3-P3, etc.) during cycling, because of larger ionic radius of Na^+. Therefore, it is necessary to enhance the structural stability of the two-dimensional material. On the other hand, in case of KIBs, it is difficult to store larger K^+ ions through the two-dimensional structure because of strong K^+–K^+ interaction. In this respect, polyanion-based compounds and Prussian blue analogues, which are composed of three-dimensionally interconnected frameworks, are more preferred in the KIB system.

Overall, research on non-lithium cathode materials remains a challenge because of their unique energy storage properties as well as consideration for commercialization. Further studies on the improvement of specific capacity, working voltage and structural stability are needed to promote the practical usage of NIBs and KIBs, therefore, the specific details for future cathode material research are as follows.

i) Rational design of cathode material in consideration of cation disordering, dopant effect, concentration of defect or moisture, etc.

ii) Realization of high electrochemical performance through surface modification, downsizing, carbon coating, etc.
iii) Elucidation of energy storage mechanism using the first-principles calculation with various advanced analyses.

Progress of research for alternate from LIBs to other alkali metal-ion batteries is not enough at this stage, nevertheless fundamental studies on the pros and cons for recently developed NIBs and KIBs could provide meaningful guidance in designing synergistic unique characteristics. We believe that this objective will be realized in the near future thanks to the remarkable advances in recent years.

Acknowledgments

This research was supported by the National Research Foundation of Korea funded by the Ministry of Science and ICT of Korea (NRF-2021R1A2C1014280, NRF-2022M3H4A1A01010832). Also, this work was supported by the Korea Institute of Materials Science (KIMS) of the Republic of Korea (No. PNK7980).

Conflict of Interest

The authors declare no conflict of interest.

Data Availability Statement

The data that support the findings of this study are available from the corresponding author upon reasonable request.

[1] J. B. Goodenough, *Energy Environ. Sci.* **2014**, *7*, 14.
[2] H. Kim, J. C. Kim, M. Bianchini, D. H. Seo, J. Rodriguez-Garcia, G. Ceder, *Adv. Energy Mater.* **2018**, *8*, 1.
[3] W. Zhang, Y. Liu, Z. Guo, *Sci. Adv.* **2019**, *5*, eaav7412.
[4] K. Kang, Y. S. Meng, J. Bréger, C. P. Grey, G. Ceder, *Science* **2006**, *311*, 977.
[5] Y. Lyu, X. Wu, K. Wang, Z. Feng, T. Cheng, Y. Liu, M. Wang, R. Chen, L. Xu, J. Zhou, Y. Lu, B. Guo, *Adv. Energy Mater.* **2021**, *11*, 2000982.
[6] N. Nitta, F. Wu, J. T. Lee, G. Yushin, *Mater. Today* **2015**, *18*, 252.
[7] Robert Rapier, The Challenges Posed By Rising Lithium Prices, *Forbes* **2021**.
[8] *Nat. Energy* **2022**, *7*, 461.
[9] N. Yabuuchi, K. Kubota, M. Dahbi, S. Komaba, *Chem. Rev.* **2014**, *114*, 11636.
[10] Y. Liu, Z. Sun, K. Tan, D. K. Denis, J. Sun, L. Liang, L. Hou, C. Yuan, *J. Mater. Chem. A* **2019**, *7*, 4353.
[11] X. Zhang, Z. Wei, K. N. Dinh, N. Chen, G. Chen, F. Du, Q. Yan, *Small* **2020**, *16*.
[12] I. Sultana, T. Ramireddy, M. M. Rahman, Y. Chen, A. M. Glushenkov, *Chem. Commun.* **2016**, *52*, 9279.
[13] London Metal Exchange, https://www.lme.com (accessed Oct 28, 2022).
[14] J. C. Pramudita, D. Sehrawat, D. Goonetilleke, N. Sharma, J. C. Pramudita, D. Sehrawat, D. Goonetilleke, N. Sharma, *Adv. Energy Mater.* **2017**, *7*, 1602911.
[15] X. Bie, K. Kubota, T. Hosaka, K. Chihara, S. Komaba, *J. Mater. Chem. A* **2017**, *5*, 4325.
[16] J.-Y. Hwang, J. Kim, T.-Y. Yu, S.-T. Myung, Y.-K. Sun, *Energy Environ. Sci.* **2018**, *11*, 2821.
[17] Q. Liu, Z. Hu, M. Chen, C. Zou, H. Jin, S. Wang, S. Chou, S. Dou, *Small* **2019**, *15*, 1805381.
[18] H. S. Hirsh, Y. Li, D. H. S. Tan, M. Zhang, E. Zhao, Y. S. Meng, *Adv. Energy Mater.* **2020**, *10*, 2001274.
[19] S. Y. Hong, Y. Kim, Y. Park, A. Choi, N.-S. Choi, K. T. Lee, *Energy Environ. Sci.* **2013**, *6*, 2067.
[20] M. Chen, Q. Liu, S. Wang, E. Wang, X. Guo, S. Chou, *Adv. Energy Mater.* **2019**, *9*, 1803609.
[21] F. Beguin, R. Setton, F. Beguin, R. Setton, A. Hamwi, P. Touzain, *Mater. Sci. Eng.* **1979**, *40*, 167.
[22] Z. Jian, W. Luo, X. Ji, *J. Am. Chem. Soc.* **2015**, *137*, 11566.
[23] S. Komaba, T. Hasegawa, M. Dahbi, K. Kubota, *Electrochem. Commun.* **2015**, *60*, 172.
[24] W. Wang, J. Zhou, Z. Wang, L. Zhao, P. Li, Y. Yang, C. Yang, H. Huang, S. Guo, W. Wang, J. Zhou, L. Zhao, P. Li, Y. Yang, C. Yang, H. Huang, S. Guo, Z. Wang, *Adv. Energy Mater.* **2018**, *8*, 1701648.
[25] J.-Y. Hwang, J. Kim, T.-Y. Yu, H.-G. Jung, J. Kim, K.-H. Kim, Y.-K. Sun, *J. Mater. Chem. A* **2019**, *7*, 21362.
[26] M. Gnana, T. Nathan, H. Yu, G.-T. Kim, J.-H. Kim, J. S. Cho, J. Kim, J.-K. Kim, M. G. T. Nathan, H. Yu, G.-T. Kim, J. Kim, J.-K. Kim, J.-H. Kim, J. S. Cho, *Adv. Sci.* **2022**, *9*, 2105882.
[27] C. Zhao, Q. Wang, Z. Yao, J. Wang, B. Sánchez-Lengeling, F. Ding, X. Qi, Y. Lu, X. Bai, B. Li, H. Li, A. Aspuru-Guzik, X. Huang, C. Delmas, M. Wagemaker, L. Chen, Y.-S. Hu, *Science* **2020**, *370*, 708.
[28] J. Xiao, F. Zhang, K. Tang, X. Li, D. Wang, Y. Wang, H. Liu, M. Wu, G. Wang, *ACS Cent. Sci.* **2019**, *5*, 1937.
[29] P.-F. Wang, H.-R. Yao, X.-Y. Liu, J.-N. Zhang, L. Gu, X.-Q. Yu, Y.-X. Yin, Y.-G. Guo, P. Wang, H. Yao, Y. Yin, Y. Guo, X. Liu, J. Zhang, L. Gu, X. Yu, *Adv. Mater.* **2017**, *29*, 1700210.
[30] S.-Y. Zhang, Y.-J. Guo, Y.-N. Zhou, X.-D. Zhang, Y.-B. Niu, E.-H. Wang, L.-B. Huang, P.-F. An, J. Zhang, X.-A. Yang, Y.-X. Yin, S. Xu, Y.-G. Guo, S. Zhang, Y. Zhou, S. Xu, Y. Guo, X. Zhang, Y. Niu, E. Wang, L. Huang, Y. Yin, Y. Guo, P. An, J. Zhang, X. Yang, *Small* **2021**, *17*, 2007236.
[31] Q. Ni, Y. Bai, F. Wu, C. Wu, *Adv. Sci.* **2017**, *4*, 1600275.
[32] H. Li, M. Xu, Z. Zhang, Y. Lai, J. Ma, *Adv. Funct. Mater.* **2020**, *30*, 2000473.
[33] P. Barpanda, L. Lander, S.-I. Nishimura, A. Yamada, P. Barpanda, L. Lander, S. Nishimura, A. Yamada, *Adv. Energy Mater.* **2018**, *8*, 1703055.
[34] T. Jin, H. Li, K. Zhu, P. F. Wang, P. Liu, L. Jiao, *Chem. Soc. Rev.* **2020**, *49*, 2342.
[35] Y. Lu, L. Wang, J. Cheng, J. B. Goodenough, *Chem. Commun.* **2012**, *48*, 6544.
[36] B. Wang, Y. Han, X. Wang, N. Bahlawane, H. Pan, M. Yan, Y. Jiang, *iScience* **2018**, *3*, 110.
[37] S. Zhao, Z. Guo, K. Yan, X. Guo, S. Wan, F. He, B. Sun, G. Wang, *Small Structures* **2021**, *2*, 2000054.
[38] C. Zhang, Y. Xu, M. Zhou, L. Liang, H. Dong, M. Wu, Y. Yang, Y. Lei, *Adv. Funct. Mater.* **2017**, *27*, 1604307.
[39] J. Qian, C. Wu, Y. Cao, Z. Ma, Y. Huang, X. Ai, H. Yang, *Adv. Energy Mater.* **2018**, *8*, 1.
[40] X. Wu, C. Wu, C. Wei, L. Hu, J. Qian, Y. Cao, X. Ai, J. Wang, H. Yang, *ACS Appl. Mater. Interfaces* **2016**, *8*, 5393.
[41] M. Tang, Y. Wu, Y. Chen, C. Jiang, S. Zhu, S. Zhuo, C. Wang, *J. Mater. Chem. A* **2019**, *7*, 486.
[42] H. Kim, J. E. Kwon, B. Lee, J. Hong, M. Lee, S. Y. Park, K. Kang, *Chem. Mater.* **2015**, *27*, 7258.
[43] H. Zhang, Y. Gao, X.-H. Liu, Z. Yang, X.-X. He, L. Li, Y. Qiao, W.-H. Chen, R.-H. Zeng, Y. Wang, S.-L. Chou, H. Zhang, S.-L. Chou, Y. Gao, X.-H. Liu, Z. Yang, X.-X. He, L. Li, Y. Qiao, Y. Wang, W.-H. Chen, R.-H. Zeng, *Adv. Funct. Mater.* **2022**, *32*, 2107718.
[44] X. Judez, L. Qiao, M. Armand, H. Zhang, *ACS Appl. Energ. Mater.* **2019**, *2*, 4008.
[45] M. Chen, Q. Liu, Y. Zhang, G. Xing, S. L. Chou, Y. Tang, *J. Mater. Chem. A* **2020**, *8*, 16061.
[46] T. Jin, P.-F. Wang, Q.-C. Wang, K. Zhu, T. Deng, J. Zhang, W. Zhang, X.-Q. Yang, L. Jiao, C. Wang, *Angew. Chem.* **2020**, *132*, 14619.
[47] C. Hakim, N. Sabi, L. A. Ma, M. Dahbi, D. Brandell, K. Edström, L. C. Duda, I. Saadoune, R. Younesi, *Commun. Chem.* **2020**, *3*, 9.
[48] P. F. Wang, Y. Xiao, N. Piao, Q. C. Wang, X. Ji, T. Jin, Y. J. Guo, S. Liu, T. Deng, C. Cui, L. Chen, Y. G. Guo, X. Q. Yang, C. Wang, *Nano Energy* **2020**, *69*, 104474.
[49] W. Zheng, Q. Liu, Z. Wang, Z. Wu, S. Gu, L. Cao, K. Zhang, J. Fransaer, Z. Lu, *Energy Storage Mater.* **2020**, *28*, 300.
[50] B. Hu, Q. Qiu, C. Li, M. Shen, B. Hu, W. Tong, K. Wang, Q. Zhou, Y. Zhang, Z. He, T. Zhang, C. Chen, *ACS Appl. Mater. Interfaces* **2022**, *14*, 28738.

[51] M. Jia, Y. Qiao, X. Li, F. Qiu, X. Cao, P. He, H. Zhou, *ACS Appl. Mater. Interfaces* **2020**, *12*, 851.
[52] X. Cao, X. Li, Y. Qiao, M. Jia, F. Qiu, Y. He, P. He, H. Zhou, *ACS Energy Lett.* **2019**, *30*, 2409.
[53] S. M. Kang, J. H. Park, A. Jin, Y. H. Jung, J. Mun, Y. E. Sung, *ACS Appl. Mater. Interfaces* **2018**, *10*, 3562.
[54] B. Song, E. Hu, J. Liu, Y. Zhang, X. Q. Yang, J. Nanda, A. Huq, K. Page, *J. Mater. Chem. A* **2019**, *7*, 1491.
[55] K. Kubota, N. Fujitani, Y. Yoda, K. Kuroki, Y. Tokita, S. Komaba, *J. Mater. Chem. A* **2021**, *9*, 12830.
[56] Y. You, S. Xin, H. Y. Asl, W. Li, P.-F. Wang, Y.-G. Guo, A. Manthiram, *Chem* **2018**, *4*, 2124.
[57] F. Ding, C. Zhao, D. Zhou, Q. Meng, D. Xiao, Q. Zhang, Y. Niu, Y. Li, X. Rong, Y. Lu, L. Chen, Y. S. Hu, *Energy Storage Mater.* **2020**, *30*, 420.
[58] L. Yu, X.-X. Xing, S.-Y. Zhang, X. Zhang, X. Han, P.-F. Wang, S. Xu, *ACS Appl. Mater. Interfaces* **2021**, *13*, 32948.
[59] T. Y. Yu, J. Kim, J. Y. Hwang, H. Kim, G. Han, H. G. Jung, Y. K. Sun, *J. Mater. Chem. A* **2020**, *8*, 13776.
[60] A. Tripathi, A. Rudola, S. R. Gajjela, S. Xi, P. Balaya, *J. Mater. Chem. A* **2019**, *7*, 25944.
[61] J. Y. Hwang, S. T. Myung, Y. K. Sun, *J. Phys. Chem. C* **2018**, *122*, 13500.
[62] J. Xun, Y. Zhang, B. Zhang, H. Xu, L. Xu, *ACS Appl. Energ. Mater.* **2020**, *3*, 6232.
[63] C. Berlanga, I. Monterrubio, M. Armand, T. Rojo, M. Galceran, M. Casas-Cabanas, *ACS Sustainable Chem. Eng.* **2020**, *8*, 725.
[64] M. Law, P. Balaya, *Energy Storage Mater.* **2018**, *10*, 102.
[65] H. Gao, I. D. Seymour, S. Xin, L. Xue, G. Henkelman, J. B. Goodenough, *J. Am. Chem. Soc.* **2018**, *140*, 18192.
[66] T. Zhu, P. Hu, C. Cai, Z. Liu, G. Hu, Q. Kuang, L. Mai, L. Zhou, *Nano Energy* **2020**, *70*, 104548.
[67] P. Ramesh Kumar, A. Kheireddine, U. Nisar, R. A. Shakoor, R. Essehli, R. Amin, I. Belharouak, *J. Power Sources* **2019**, *429*, 149.
[68] L. Tang, X. Liu, Z. Li, X. Pu, J. Zhang, Q. Xu, H. Liu, Y.-G. Wang, Y. Xia, *ACS Appl. Mater. Interfaces* **2019**, *11*, 27813.
[69] R. Rajagopalan, Z. Wu, Y. Liu, S. Al-Rubaye, E. Wang, C. Wu, W. Xiang, B. Zhong, X. Guo, S. X. Dou, H. K. Liu, *J. Power Sources* **2018**, *398*, 175.
[70] M. Chen, D. Cortie, Z. Hu, H. Jin, S. Wang, Q. Gu, W. Hua, E. Wang, W. Lai, L. Chen, S.-L. Chou, X.-L. Wang, S.-X. Dou, *Adv. Energy Mater.* **2018**, *8*, 1800944.
[71] A. Plewa, A. Kulka, D. Baster, J. Molenda, *Solid State Ionics* **2019**, *335*, 15.
[72] Y. Fang, Q. Liu, X. Feng, W. Chen, X. Ai, L. Wang, L. Wang, Z. Ma, Y. Ren, H. Yang, Y. Cao, *J. Energy Chem.* **2021**, *54*, 564.
[73] Z.-Y. Chen, X.-Y. Fu, L.-L. Zhang, B. Yan, X.-L. Yang, *ACS Appl. Mater. Interfaces* **2022**, *14*, 5506.
[74] B. Xie, L. Wang, J. Shu, X. Zhou, Z. Yu, H. Huo, Y. Ma, X. Cheng, G. Yin, P. Zuo, *ACS Appl. Mater. Interfaces* **2019**, *11*, 46705.
[75] J. Peng, J. Wang, H. Yi, W. J. Hu, Y. Yu, J. Yin, Y. Shen, Y. Liu, J. Luo, Y. Xu, P. Wei, Y. Li, Y. Jin, Y. Ding, L. Miao, J. Jiang, J. Han, Y. Huang, *Adv. Energy Mater.* **2018**, *8*, 1702856.
[76] Y. Shang, X. Li, J. Song, S. Huang, Z. Yang, Z. J. Xu, H. Y. Yang, *Chem* **2020**, *6*, 1804.
[77] Y. Xu, J. Wan, L. Huang, M. Ou, C. Fan, P. Wei, J. Peng, Y. Liu, Y. Qiu, X. Sun, C. Fang, Q. Li, J. Han, Y. Huang, J. A. Alonso, Y. Zhao, *Adv. Energy Mater.* **2019**, *9*, 1803158.
[78] M. Qin, W. Ren, R. Jiang, Q. Li, X. Yao, S. Wang, Y. You, L. Mai, *ACS Appl. Mater. Interfaces* **2021**, *13*, 4007.
[79] X. Zhang, Y. Yang, X. Qu, Z. Wei, G. Sun, K. Zheng, H. Yu, F. Du, *Adv. Funct. Mater.* **2019**, *29*, 1905679.
[80] T. Deng, X. Fan, J. Chen, L. Chen, C. Luo, X. Zhou, J. Yang, S. Zheng, C. Wang, *Adv. Funct. Mater.* **2018**, *28*, 1800219.
[81] T. Masese, K. Yoshii, Y. Yamaguchi, T. Okumura, Z.-D. Huang, M. Kato, K. Kubota, J. Furutani, Y. Orikasa, H. Senoh, H. Sakaebe, M. Shikano, *Nat. Commun.* **2018**, *9*, 3823.
[82] Y. S. Xu, Y. N. Zhou, Q. H. Zhang, M. Y. Qi, S. J. Guo, J. M. Luo, Y. G. Sun, L. Gu, A. M. Cao, L. J. Wan, *Chem. Eng. J.* **2021**, *412*, 128735.
[83] Y. S. Xu, Q. H. Zhang, D. Wang, J. C. Gao, X. Sen Tao, Y. Liu, Y. G. Sun, L. Gu, B. B. Chang, C. T. Liu, S. Q. Shi, A. M. Cao, *Energy Storage Mater.* **2020**, *31*, 20.
[84] J. Weng, J. Duan, C. Sun, P. Liu, A. Li, P. Zhou, J. Zhou, *Chem. Eng. J.* **2020**, *392*, 123649.
[85] J. U. Choi, J. Kim, J. Y. Hwang, J. H. Jo, Y. K. Sun, S. T. Myung, *Nano Energy* **2019**, *61*, 284.
[86] B. Peng, Y. Li, J. Gao, F. Zhang, J. Li, G. Zhang, *J. Power Sources* **2019**, *437*, 226913.
[87] Z. Xiao, F. Xia, L. Xu, X. Wang, J. Meng, H. Wang, X. Zhang, L. Geng, J. Wu, L. Mai, Z. Xiao, F. Xia, J. Meng, H. Wang, X. Zhang, L. Geng, J. Wu, L. Mai, L. Xu, X. Wang, L. M. Foshan, *Adv. Funct. Mater.* **2022**, *32*, 2108244.
[88] Z. Xiao, J. Meng, F. Xia, J. Wu, F. Liu, X. Zhang, L. Xu, X. Lin, L. Mai, *Energy Environ. Sci.* **2020**, *13*, 3129.
[89] N. Naveen, S. C. Han, S. P. Singh, D. Ahn, K.-S. Sohn, M. Pyo, *J. Power Sources* **2019**, *430*, 137.
[90] H. Kim, D. H. Seo, A. Urban, J. Lee, D. H. Kwon, S. H. Bo, T. Shi, J. K. Papp, B. D. McCloskey, G. Ceder, *Chem. Mater.* **2018**, *30*, 6532.
[91] N. Naveen, W. B. Park, S. P. Singh, S. C. Han, D. Ahn, K.-S. Sohn, M. Pyo, *Small* **2018**, *14*, 1803495.
[92] J. Liao, Q. Hu, B. Che, X. Ding, F. Chen, C. Chen, *J. Mater. Chem. A* **2019**, *7*, 15244.
[93] H. Park, H. Kim, W. Ko, J. H. Jo, Y. Lee, J. Kang, I. Park, S.-T. Myung, J. Kim, *Energy Storage Mater.* **2020**, *28*, 47.
[94] J. Kang, H. Park, W. Ko, Y. Lee, J. Ahn, J.-K. Yoo, S. H. Song, H. Kim, J. Kim, *J. Mater. Chem. A* **2021**, *9*, 9898.
[95] J. Wang, B. Ouyang, H. Kim, Y. Tian, G. Ceder, H. Kim, *J. Mater. Chem. A* **2021**, *9*, 18564.
[96] S. S. Fedotov, N. D. Luchinin, D. A. Aksyonov, A. V. Morozov, S. V. Ryazantsev, M. Gaboardi, J. R. Plaisier, K. J. Stevenson, A. M. Abakumov, E. V. Antipov, *Nat. Commun.* **2020**, *11*, 1484.
[97] J. Bodart, N. Eshraghi, T. Carabin, B. Vertruyen, R. Cloots, F. Boschini, A. Mahmoud, *J. Power Sources* **2020**, *480*, 229057.
[98] Z. Zhang, R. Wang, Z. Chen, X. Liu, Z. Liu, J. Zeng, X. Zhao, K. Peng, Q. Yao, X. Zhang, K. Shi, C. Zhu, X. Yan, *Chem. Eng. J.* **2022**, *436*, 135235.
[99] X. Lin, J. Huang, H. Tan, J. Huang, B. Zhang, *Energy Storage Mater.* **2019**, *16*, 97.
[100] W. Ko, H. Park, J. H. Jo, Y. Lee, J. Kang, Y. H. Jung, T.-Y. Jeon, S.-T. Myung, J. Kim, *Nano Energy* **2019**, *66*, 104184.
[101] J. Kang, W. Ko, H. Park, Y. Lee, J. H. Jo, J. U. Choi, S. T. Myung, J. Kim, *Energy Storage Mater.* **2020**, *33*, 276.
[102] L. Li, Z. Hu, Y. Lu, C. Wang, Q. Zhang, S. Zhao, J. Peng, K. Zhang, S. L. Chou, J. Chen, *Angew. Chem. Int. Ed.* **2021**, *60*, 13050.
[103] S. Chong, J. Yang, L. Sun, S. Guo, Y. Liu, H. K. Liu, *ACS Nano* **2020**, *14*, 9807.
[104] B. Huang, Y. Liu, Z. Lu, M. Shen, J. Zhou, J. Ren, X. Li, S. Liao, *ACS Sustainable Chem. Eng.* **2019**, *7*, 16659.
[105] Y. H. Zhu, X. Yang, D. Bao, X. F. Bie, T. Sun, S. Wang, Y. S. Jiang, X. B. Zhang, J. M. Yan, Q. Jiang, *Joule* **2018**, *2*, 736.
[106] L. Deng, J. Qu, X. Niu, J. Liu, J. Zhang, Y. Hong, M. Feng, J. Wang, M. Hu, L. Zeng, Q. Zhang, L. Guo, Y. Zhu, *Nat. Commun.* **2021**, *12*, 2167.
[107] M. Qin, W. Ren, J. Meng, X. Wang, X. Yao, Y. Ke, Q. Li, L. Mai, *ACS Sustainable Chem. Eng.* **2019**, *7*, 11564.
[108] B. Huang, Y. Shao, Y. Liu, Z. Lu, X. Lu, S. Liao, *ACS Appl. Energ. Mater.* **2019**, *2*, 6528.
[109] H. Kim, D. H. Seo, M. Bianchini, R. J. Clément, H. Kim, J. C. Kim, Y. Tian, T. Shi, W. S. Yoon, G. Ceder, *Adv. Energy Mater.* **2018**, *8*, 1.
[110] W. Lee, J. Kim, S. Yun, W. Choi, H. Kim, W.-S. Yoon, *Energy Environ. Sci.* **2020**, *13*, 4406.
[111] C. Ling, J. Chen, F. Mizuno, *J. Phys. Chem. C* **2013**, *117*, 21158.
[112] X. Liu, Y. Cao, J. Sun, *Adv. Energy Mater.* **2022**, *12*, 2202532.
[113] G.-H. Lee, J. Wu, D. Kim, K. Cho, M. Cho, W. Yang, Y.-M. Kang, *Angew. Chem.* **2020**, *132*, 8759.
[114] W. Lee, S. Yun, H. Li, J. Kim, H. Lee, K. Kwon, J. Yong Lee, Y.-M. Choi, W.-S. Yoon, W. Lee, S. Yun, J. Kim, H. Lee, K. Kwon, W. Yoon, H. Li, J. Y. Lee, Y. Choi, *Small* **2020**, *16*, 1905875.
[115] K. Luo, M. R. Roberts, R. Hao, N. Guerrini, D. M. Pickup, Y. S. Liu, K. Edström, J. Guo, A. V. Chadwick, L. C. Duda, P. G. Bruce, *Nat. Chem.* **2016**, *8*, 684.
[116] D.-H. Seo, J. Lee, A. Urban, R. Malik, S. Kang, G. Ceder, *Nat. Chem.* **2016**, *8*, 692.
[117] M. Jia, H. Li, Y. Qiao, L. Wang, X. Cao, J. Cabana, H. Zhou, *ACS Appl. Mater. Interfaces* **2020**, *12*, 38249.
[118] Q. Yang, P.-F. Wang, J.-Z. Guo, Z.-M. Chen, W.-L. Pang, K.-C. Huang, Y.-G. Guo, X.-L. Wu, J.-P. Zhang, *ACS Appl. Mater. Interfaces* **2018**, *10*, 34272.
[119] Y. Wang, R. Xiao, Y. S. Hu, M. Avdeev, L. Chen, *Nat. Commun.* **2015**, *6*, 1.
[120] L. Zhang, J. Wang, G. Schuck, F. Xi, L. Du, M. Winter, G. Schumacher, J. Li, *Small Methods* **2020**, *4*, 2000422.
[121] Y.-U. Park, D.-H. Seo, B. Kim, K.-P. Hong, H. Kim, S. Lee, R. A. Shakoor, K. Miyasaka, J.-M. Tarascon, K. Kang, *Sci. Rep.* **2012**, *2*, 704.

[122] P. Serras, V. Palomares, J. Alonso, N. Sharma, J. M. López Del Amo, P. Kubiak, M. L. Fdez-Gubieda, T. Rojo, *Chem. Mater.* **2013**, *25*, 4917.
[123] Z. Jian, W. Han, X. Lu, H. Yang, Y.-S. Hu, J. Zhou, Z. Zhou, J. Li, W. Chen, D. Chen, L. Chen, *Adv. Energy Mater.* **2013**, *3*, 156.
[124] H. Li, H. Tang, C. Ma, Y. Bai, J. Alvarado, B. Radhakrishnan, S. P. Ong, F. Wua, Y. S. Meng, C. Wu, *Chem. Mater.* **2018**, *30*, 2498.
[125] J. Kang, H. Park, H. Kim, J. H. Jo, W. Ko, Y. Lee, S. Myung, J. Kim, *ACS Sustainable Chem. Eng.* **2020**, *8*, 163.
[126] C. Xu, R. Xiao, J. Zhao, F. Ding, Y. Yang, X. Rong, X. Guo, C. Yang, H. Liu, B. Zhong, Y. S. Hu, *ACS Energy Lett.* **2022**, *7*, 97.
[127] H. Li, Z. Zhang, M. Xu, W. Bao, Y. Lai, K. Zhang, J. Li, *ACS Appl. Mater. Interfaces* **2018**, *10*, 24564.
[128] B. Shen, M. Xu, Y. Niu, J. Han, S. Lu, J. Jiang, Y. Li, C. Dai, L. Hu, C. Li, *ACS Appl. Mater. Interfaces* **2018**, *10*, 502.
[129] M. Chen, L. Chen, Z. Hu, Q. Liu, B. Zhang, Y. Hu, Q. Gu, J.-L. Wang, L.-Z. Wang, X. Guo, S.-L. Chou, S.-X. Dou, *Adv. Mater.* **2017**, *29*, 1605535.
[130] Y. Tang, W. Li, P. Feng, M. Zhou, K. Wang, K. Jiang, *Chem. Eng. J.* **2020**, *396*, 125269.
[131] X. Wu, D. P. Leonard, X. Ji, *Chem. Mater.* **2017**, *29*, 5031.
[132] M. Jiang, Z. Hou, J. Wang, L. Ren, Y. Zhang, J. G. Wang, *Nano Energy* **2022**, *102*, 107708.
[133] X. Wu, Y. Luo, M. Sun, J. Qian, Y. Cao, X. Ai, H. Yang, *Nano Energy* **2015**, *13*, 117.
[134] J. Song, L. Wang, Y. Lu, J. Liu, B. Guo, P. Xiao, J. J. Lee, X. Q. Yang, G. Henkelman, J. B. Goodenough, *J. Am. Chem. Soc.* **2015**, *137*, 2658.
[135] W. Wang, Y. Gang, Z. Hu, Z. Yan, W. Li, Y. Li, Q. F. Gu, Z. Wang, S. L. Chou, H. K. Liu, S. X. Dou, *Nat. Commun.* **2020**, *11*, 1.
[136] B. Xie, L. Wang, H. Li, H. Huo, C. Cui, B. Sun, Y. Ma, J. Wang, G. Yin, P. Zuo, *Energy Storage Mater.* **2021**, *36*, 99.
[137] C. Y. Chen, J. Rizell, G. M. Kanyolo, T. Masese, Y. Sassa, M. Månsson, K. Kubota, K. Matsumoto, R. Hagiwara, Q. Xu, *Chem. Commun.* **2020**, *56*, 9272.
[138] Z. Hu, M. Weng, Z. Chen, W. Tan, S. Li, F. Pan, *Nano Energy* **2021**, *83*, 105834.
[139] Q. Zhang, C. Didier, W. Kong Pang, Y. Liu, Z. Wang, S. Li, V. K. Peterson, J. Mao, Z. Guo, S. Li, V. K. Peterson, Z. Guo, Q. Zhang, C. Didier, W. K. Pang, Y. Liu, Z. Wang, J. Mao, *Adv. Energy Mater.* **2019**, *9*, 1900568.
[140] N. Sharma, P. Serras, V. Palomares, H. E. A. Brand, J. Alonso, P. Kubiak, M. L. Fdez-Gubieda, T. Rojo, *Chem. Mater.* **2014**, *26*, 3391.
[141] Y.-U. Park, D.-H. Seo, H.-S. Kwon, B. Kim, J. Kim, H. Kim, I. Kim, H.-I. Yoo, K. Kang, *J. Am. Chem. Soc.* **2013**, *135*, 13870.
[142] C. Xu, Z. Yang, X. Zhang, M. Xia, H. Yan, J. Li, H. Yu, L. Zhang, J. Shu, *Nano-Micro Lett.* **2021**, *13*, 166.
[143] J. Kim, H. Lee, H. Cha, M. Yoon, M. Park, J. Cho, *Adv. Energy Mater.* **2018**, *8*, 1702028.
[144] Y. You, H. Celio, J. Ianyu Li, A. Dolocan, A. Manthiram, *Angew. Chem.* **2018**, *130*, 6590.

Manuscript received: November 7, 2022
Revised manuscript received: December 15, 2022
Accepted manuscript online: December 15, 2022
Version of record online: January 10, 2023